



University of Crete  
Physics Department



FO.R.T.H.  
Institute of Electronic Structure  
and Laser

# **Characterization of Low-Order Harmonics generated with the Interferometric Polarization Gating Technique**

**Dimitrios Rompotis**

MSc Thesis

Supervisor : Prof. Dr. Dimitris Charalambidis

Advisor : Dr. Paraskevas Tzallas

Iraklion 2011

# Contents

<b>Acknowledgements</b>	<b>3</b>
<b>Introduction</b>	<b>4</b>
<b>1 Generation of Attosecond Laser Pulses</b>	<b>5</b>
1.1 High-Order Harmonic Generation (HHG) . . . . .	5
1.1.1 Generating Field Polarization Effects . . . . .	7
1.2 Attosecond Pulse Trains . . . . .	8
1.3 Isolated Attosecond Pulses . . . . .	9
<b>2 Interferometric Polarization Gating</b>	<b>10</b>
2.1 Concept of the IPG technique . . . . .	10
2.2 Double Mach-Zehnder Polarization Gating Setup . . . . .	11
2.3 Low-Order Harmonic Generation with the IPG technique . . . . .	13
<b>3 Generation of a Third-Harmonic Pulse with the IPG technique</b>	<b>15</b>
3.1 The experimental setup . . . . .	15
3.1.1 The Ti:Sapphire Laser System . . . . .	15
3.1.2 High-harmonic generation experimental setup . . . . .	17
3.1.3 Third-harmonic characterization experimental setup . . . . .	18
3.2 Spectral Characterization of the Third-Harmonic Pulse . . . . .	20
3.3 Temporal Characterization of the Third-Harmonic Pulse . . . . .	21
3.3.1 The $2^{nd}$ Order Intensity Volume Autocorrelation Technique . . . . .	21
3.3.2 The Non-Linear Medium . . . . .	23
3.3.3 Split-Mirror Focal Spot . . . . .	24
3.3.4 $2^{nd}$ Order Intensity Volume Autocorrelation Measurement of the Third-Harmonic Pulse . . . . .	26
3.4 Conclusions - Future Plans . . . . .	29
<b>A Mathematica Code for the Ellipticity Modulated Pulse Calculations</b>	<b>30</b>
<b>B Experimental Setup Photographs</b>	<b>36</b>

# Acknowledgements

I would like to take the opportunity to thank all the people that supported me during my Master of Science studies at the Physics Department of the University of Crete and helped to successfully complete the work presented in this thesis.

First of all, I would like to thank my supervisor Prof. Dimitris Charalambidis for giving me the opportunity to work in the Attosecond Science group in the Institute of Electronic Structure and Lasers in FORTH and also for his kind support throughout my experimental studies in Crete.

Furthermore I would like to specially thank my advisor Dr. Paraskevas Tzallas for his guidance and supervision of my experimental work. His effort and expertise have been really inspiring to me and made a big contribution to the experimental skills I gained during these years in Crete. I would also like to thank Dr. Stelios Tzortzakis for the financial support during the last months of my MSc course and Prof. Iannis Komninos for being in my MSc thesis committee.

One person that I want to particularly thank for his help and support inside the lab and also in real life is Manolis Skantzakis. The calculations presented in this thesis made possible by his help and guidance.

The maintenance of the laser system was very important for the experimental part of my thesis and I would like to thank Panos Siozos for this reason.

I would also like to thank the people that helped me inside the lab with their physical presence and ideas, Jann Kruse, Paolo Carpeggiani, Giorgos Kolliopoulos and Kyriaki Kosma.

Additionally I would like to thank my fellow MSc Diploma students for their encouragement and the fun moments we had during our MSc course.

Finally I would like to thank my family for being supportive even at the darkest hours, Anastasia for the inspiration that gave me in the most difficult times during the last years and of course my friends for the great moments outside the scientific environment that gave me strength and balance all the years that I spent in Crete.

# Introduction

Light pulses have provided the means for observing fast-evolving processes since the invention of photography. The evolution of ultrafast processes in the molecular and even atomic level can be tracked by means of ultrashort laser pulses with the widely used pump-probe technique. A pump laser pulse initiates the dynamics to be observed followed by a delayed probe pulse that probes the evolution of the process as a function of the delay introduced between the pump and the probe pulse. The time resolution that can be achieved with this technique is determined by the laser pulse duration.

During the last decades, continuous efforts in laser-pulse engineering reached femtosecond and lately attosecond pulse durations allowing with the tracking of ultrafast molecular and atomic dynamics. High-power ultrafast laser systems are today based on Ti:Sapphire crystals emitting pulses with a central wavelength of 800 nanometers and pulse durations in the femtosecond regime. Low odd-order harmonics of these systems are routinely generated through the interaction with a gas phase medium and can be utilized for time-resolved studies of photochemical reactions as many organic molecules absorb in this wavelength range. The low-order harmonic pulse duration is proportional to the generating fundamental pulse duration and determines the temporal resolution that can be achieved in this kind of experiments.

The scope of the present thesis is the utilization of the previously developed Interferometric Polarization Gating technique for generation of ultrashort low-order harmonic pulses. Taking advantage of the harmonic generation dependence on the generating pulse polarization properties, a temporal gate can be formed in which low-order harmonic emission takes place. In this case the temporal gate width defines the low-order harmonic pulse duration instead of the longer generating infrared pulse duration and as a result shorter harmonic pulses can be generated.

The present thesis deals with the generation and characterization of a third-harmonic pulse using the Interferometric Polarization Gating technique. In the first part the parameters for the application of the Interferometric Polarization Gating technique for low-order harmonic pulse generation are investigated. The second part of this thesis deals with the experimental implementation of this approach for the generation of an intense ultrashort third-harmonic pulse of a Ti:Sapphire laser system.

# Chapter 1

## Generation of Attosecond Laser Pulses

According to Fourier synthesis, a pulse of a given duration is formed as a superposition of a number of spectral components, with an appropriate spectral phase relation. The pulse duration and spectral width are related as:

$$\Delta\nu \cdot \Delta t \geq K \quad (1.1)$$

where  $\Delta\nu$  denotes the spectral width,  $\Delta t$  the pulse duration,  $K$  is a constant that depends on the pulse shape ( $K = 0.441$  for a Gaussian temporal shape) and the equality part corresponds to the shortest pulse duration that can be achieved using this spectral bandwidth. Phase-locking the pulse spectral components is essential as random phases will prohibit short pulse formation. From equation 1.1 it is evident that a 10 fsec bandwidth-limited laser pulse corresponds to a spectral width of approximately 50 THz. In order to reduce the pulse duration to the attosecond timescale an enormous bandwidth is needed (25 asec  $\rightarrow$  20 PHz).

As proposed by [1] the broad bandwidth needed to support attosecond pulses can be provided by means of high-order harmonics of the fundamental laser pulse frequency. High-order harmonics are generated when an intense laser pulse interacts with an atomic sample [2],[3], reaching soft x-ray wavelengths in particular cases [4],[5]. The generation mechanism and the spectral characteristics of high-order harmonics are discussed below in a qualitative way.

### 1.1 High-Order Harmonic Generation (HHG)

Generation of high-order harmonics is commonly achieved by focusing a many-cycle linearly-polarized intense ultrashort laser pulse below the tip of a pulsed gas nozzle, that provides the generating gas-phase medium, in a vacuum chamber. The generated harmonics propagate in the same direction as the generating beam with a smaller angular spread, that in general depends on the harmonic order. In this case only odd-order harmonics are observed because of the electric dipole approximation selection rules and the symmetry of the atomic potential.

The high-order harmonic spectrum exhibits a generic shape. There is a sharp decline in the intensity of the first few lower-order harmonics, followed by a plateau where the harmonic intensity is nearly constant for several orders, when the harmonic photon energy becomes equal or larger than than the ionization energy of the medium and eventually an abrupt cut-off.

A perturbative description is not adequate to explain the nearly constant conversion efficiency in the plateau region of the high-order harmonic spectrum, as lowest-order perturbation theory predicts a drop in conversion efficiency with growing orders.

In general the conversion efficiency for high-order harmonics can be at most of the order of  $10^{-5}$  in the case of the "plateau" harmonics generated by atomic gas targets [7] and can reach values up to  $10^{-2}$  with the use of surface targets [6].

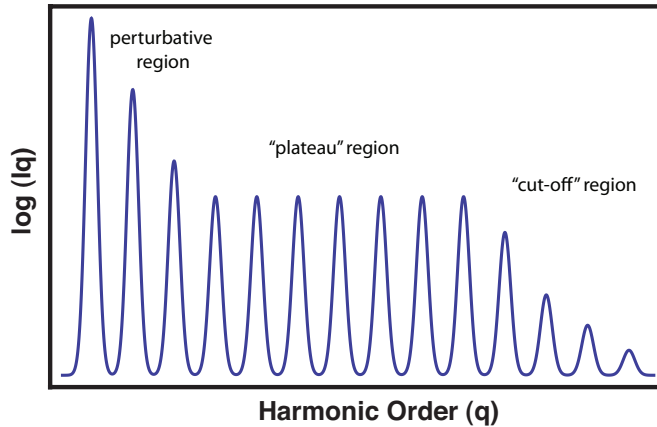


Figure 1.1: A typical high-order harmonic spectrum exhibiting a perturbative region of decreasing harmonic intensity with increasing order, followed by a constant conversion efficiency "plateau" region, ending in a sharp "cut-off" region where the harmonic intensity decreases rapidly.

High-order harmonic generation can be described in an intuitive way by a quasi-classical model introduced in Ref. [7]. A more rigorous quantum theory retaining the basic elements of this model was later formulated in Ref. [8].

According to this model, high-order harmonic generation is described as a three step process where an atom is first ionized by the intense laser pulse, subsequently the liberated electron is accelerated by the force exerted on it by the pulse electric field and finally recombines with the parent ion emitting coherent radiation that carries away the excessive kinetic energy gained during the electron excursion in the pulse electric field.

When a very intense low-frequency laser pulse interacts with an atom, the latter can be ionized with a certain probability absorbing multiple low-frequency photons. This process is called multi-photon ionization and up to a certain pulse intensity can be described by perturbation theory methods. When the laser pulse intensity approaches or even exceeds the atomic unit of intensity ( $I_{at} \approx 3.5 \times 10^{16} W/cm^2$  for the hydrogen atom), it is able to distort the atomic binding potential to such an extent that the electron can be liberated, with a finite probability,

by tunnelling through the formed potential barrier or over the barrier for higher pulse intensity values. The probability for ionization can be shown that becomes maximum near the pulse electric field local maxima [9].

Immediately after being liberated by the atomic binding potential the electron is subjected to the pulse electric field. The electron is accelerated away from the core but as the pulse electric field rapidly changes sign it is driven back towards the core direction. Within a fraction of half the laser pulse period the electron may revisit the parent ion to recombine and emit a burst of continuum XUV radiation. As this process is repeated periodically the emitted spectrum consists of an XUV frequency comb of the odd-order harmonics of the fundamental laser pulse frequency as described above. The highest harmonic photon energy corresponds to the maximum kinetic energy of the recombining electrons and therefore defines the harmonic spectrum cut-off [10]:

$$\hbar\omega_{max} = I_p + 3.17U_p \quad (1.2)$$

where  $I_p$  is the ionization potential of the generating gas and  $U_p$  corresponds to the mean electron quiver energy in the pulse electric field, known also as ponderomotive energy.

Experimentally, high-order harmonics are generated from a macroscopic gas medium where the high-order harmonic spectrum builds up from the coherent superposition of the emitted fields throughout the generating medium. Therefore several propagation effects have to be taken into account, namely dispersion introduced by the ionized generating medium and geometrical effects due to the laser pulse focusing, in order to achieve good phase-matching conditions for efficient generation.

### 1.1.1 Generating Field Polarization Effects

One very important characteristic for the scope of this thesis is the dependence of high harmonic generation on the polarization properties of the generating field. In general harmonic generation is very sensitive to the generating pulse polarization and the harmonic intensity rapidly drops with increasing ellipticity ( $\epsilon$ ) of the generating field. As evident from the above discussion the electron, once liberated in the continuum will follow a trajectory depending on the driving electric field orientation and phase. In a classical-trajectory perspective, the escaping electron in an elliptically polarized electric field may never re-encounter the parent ion and as a consequence no radiation will be emitted. In a quantum mechanical perspective, the electron wave-packet has a finite probability of recombining with the parent ion owing to its transverse spread while being free from the atomic binding potential. According to the lowest-order perturbation theory the harmonic intensity scales as a function of the generating field ellipticity as [11],[12]:

$$I_q \propto \left( \frac{1 - \epsilon^2}{1 + \epsilon^2} \right)^{(q-1)} \quad (1.3)$$

where  $q$  corresponds to the harmonic order and  $\epsilon$  to the laser pulse electric field ellipticity value.

For a linearly polarized generating pulse where the value of ellipticity is zero, harmonic intensity takes its maximum value ( $I_{q_{max}}$ ) while in the case of circular polarization  $\epsilon = 1$  and the harmonic intensity drops to zero.

An ellipticity threshold ( $\epsilon_{th}$ ) can be defined as the value of ellipticity above which  $I_q < I_{q_{max}}/2$ . Equation 1.2 can be valid in the non-perturbative regime if the nonlinearity order ( $p$ ) instead of the harmonic order is used. In this case the nonlinearity order is equal to the harmonic order for the first few low-order harmonics, takes a constant value for the "plateau" harmonics ( $5 \leq p \leq 8$ ) and scales approximately as  $p \approx 16$  in the cut-off region [9],[13]. For the needs of the present work the ellipticity threshold for the third harmonic corresponds to  $\epsilon_{th_{3dH}} = 0.414$  as calculated from equation 1.3 where the ellipticity threshold for high-order harmonics used for the generation of isolated attosecond laser pulses reaches the value of  $\epsilon_{th_{HOH}} = 0.15$ .

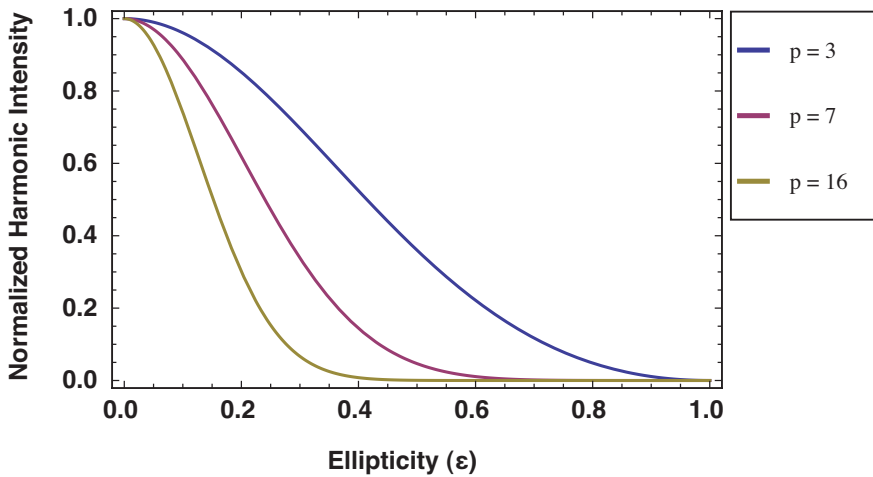


Figure 1.2: Harmonic intensity as a function of the driving laser field ellipticity is shown for three different nonlinearity orders as predicted by eq. 1.3. The harmonic intensity drops rapidly with increasing ellipticity and the distribution becomes steeper with growing order of nonlinearity.

## 1.2 Attosecond Pulse Trains

As proposed by [1], [14] in analogy with the mode-locked laser operation principle, where phase-locking of the axial modes of the laser cavity results to the generation of a train of ultrashort laser pulses, a spectral comb of sufficient bandwidth properly phase-locked could be used for the synthesis of a sub-femtosecond pulse train. In this case the required bandwidth to support attosecond pulse formation can be available by means of the high-order harmonic frequency comb.

When fulfilling the appropriate phase-matching conditions, taking into account the atomic as well as the macroscopic response of the generating medium leading to phase-locking between the harmonics and by using a filter to select a group of harmonics blocking at the same time the fundamental generating pulse, an attosecond pulse train is formed with the individual pulses of

the train being separated by half of the fundamental laser period. Attosecond pulse train sources have been utilized in non-linear autocorrelation diagnostics or XUV pump-probe applications [15], [16], [17], [18].

### 1.3 Isolated Attosecond Pulses

For many applications of attosecond pulses would be desirable to be able to select a single pulse from the generated pulse train just as a single pulse can be extracted from a mode-locked pulse train with the use of a Pockels cell.

As mentioned above, the pulses formed in an attosecond pulse train are spaced in time by half of the fundamental laser pulse period, which for the commonly used Ti:S laser systems with a central wavelength of 800 nm corresponds to about 1.33 femtoseconds. Consequently the extraction of a pulse from the attosecond pulse train is impossible by electronic means due to their limited speed.

Despite the fact that pulse picking is inevitable, an isolated attosecond pulse is generated if the XUV emission can be restricted within half of the optical cycle of the generating laser pulse. In this case a coherent continuum is emitted by the generating medium corresponding to a single pulse. Two main experimental approaches that take advantage of the above mentioned process exist for the generation of isolated attosecond pulses.

The first utilizes a few-cycle driving laser pulse where the emitted XUV spectrum is quasi-continuum with a pure continuum part in the cut-off region generated by the half cycle of the few-cycle laser field with the highest amplitude. With the use of a thin metal filter the cut-off spectral region can be selected corresponding to one isolated attosecond pulse. Isolated attosecond pulses generated with this technique have so far low pulse energy due to the limited power delivered by few-cycle laser systems. Development of high-peak power few-cycle laser systems is thus required for energetic isolated attosecond pulses generated with this approach. The second approach based on a proposition presented in [19] gives the ability to make use of commercially available many-cycle high-peak power laser systems where a temporal gate near the peak of the pulse envelope restricts the XUV radiation emission to occur during a part of the generating field. This temporal gate formation is based on the dependence of high harmonic generation on the ellipticity of the generating laser field as described in the previous section. Modulating the pulse polarization in a way where the pulse ellipticity will be below the threshold value ( $\epsilon_{th}$ ) for only a half-cycle of the generating field at the peak of the pulse envelope, a temporal gate is created defining a time interval ( $\tau_g$ ) during which XUV emission will take place. The generating pulse in this case consists of a linearly polarized half-cycle central part turning to elliptically polarized towards its tails. Several experimental implementation approaches exist for the generation of such a polarization-modulated pulse. For the needs of the present work the interferometric polarization gating (IPG) technique has been used and will be analyzed in detail in the following chapter.

## Chapter 2

# Interferometric Polarization Gating

The Interferometric Polarization Gating Technique (IPG) can be utilized for the generation of intense isolated attosecond laser pulses by many-cycle intense driving laser fields as described above and has been successfully implemented for the generation of coherent continuum XUV radiation supporting the synthesis of intense isolated attosecond pulses.

In the present work the IPG technique is used for the generation of ultrashort intense low-order harmonic pulses. As described in the previous section a temporal gate based on the ellipticity properties of the generating field defines the time interval during which harmonic generation takes place. In this case the ellipticity threshold for a given harmonic defines the time interval for efficient generation of the particular harmonic. An intense ultrashort harmonic pulse can then be spectrally selected from the emitted radiation. The objective of the present work is the generation and characterization of an intense ultrashort third-harmonic pulse of a Ti:S laser system generated with the IPG technique.

### 2.1 Concept of the IPG technique

The basic concept of the interferometric polarization gating technique for the formation of an ellipticity modulated laser pulse is described below.

A linearly polarized laser pulse with duration  $\tau_L$  is first split into two identical perpendicularly polarized parts.

The first of these two pulses is split also in two equal parts and an odd number of laser wavelengths delay ( $\delta$ ) is introduced between them so that a destructive interference minimum is formed in the center of the pulse after the two parts recombine.

The second pulse is also split into two equal parts and a delay ( $\Delta t$ ) of the same order of magnitude is introduced between them, such as the two parts interfere constructively when they recombine.

The destructively ( $E_{des}$ ) and constructively ( $E_{con}$ ) interfering waveforms are then superimposed to form an ellipticity modulated laser pulse with linear polarization in its central part, where the one waveform exhibits the destructive interference minimum, and elliptical polarization with varying ellipticity towards its tails.

The temporal gate width can be controlled by the delays introduced between the pairs of pulses  $\delta$  and  $\Delta t$  and by the ratio of the two overlapping components  $E_{con}/E_{des}$  that form the ellipticity modulated pulse. This concept has been implemented by using a double Michelson interferometer arrangement [20] and later by a double Mach-Zehnder interferometer arrangement [21] which increases the energy content of the temporal gate  $\tau_g$  by a factor of 2 compared to the double Michelson interferometer arrangement but gives limited control of the amplitudes of the two pairs of pulses. In this work the double Mach-Zehnder interferometer arrangement has been used and will be analyzed in detail in the next paragraph.

## 2.2 Double Mach-Zehnder Polarization Gating Setup

The double Mach-Zehnder polarization gating arrangement is shown schematically below. A laser pulse is initially split in two identical parts by the first beam splitter BS1. The transmitted and reflected parts are delayed by a multiple of half the laser pulse period, with the use of a pair of tilted BK7 plates (P1, P2) controlled by two New Focus Picomotor modules. The two plates are at a slightly different angle with respect to the beam propagation axis and the two pulses are delayed as a result of the difference in the corresponding optical paths.

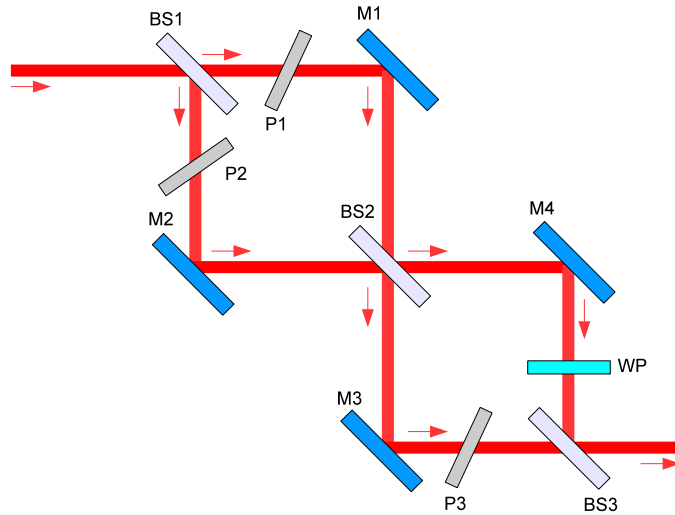


Figure 2.1: Double Mach-Zehnder IPG arrangement. M1, M2, M3, M4: IR Reflecting Mirrors, BS1, BS2: 50:50 Beam Splitters, BS3 R:20% T:80% Beam Splitter, P1,P2,P3: BK7 Delay plates.

The two delayed pulses are combined in the second beam splitter BS2 where a constructively interfering part ( $E_{con}$ ) is transmitted and a part exhibiting a destructive interference minimum in the center ( $E_{des}$ ) is reflected.

The polarization of the constructively interfering part is then rotated, to be perpendicular to the initial polarization of the pulse, by a zero-order half-wave plate (WP) after being reflected from the M4 mirror. The half-wave plate and a third plate (P3), also on a Picomotor tilting stage, introduce a  $\pi/2$  phase shift between the two components. The two waveforms ( $E_{des}$  and  $E_{con}$ ) are then recombined in a 20% reflection 80% transmission beam splitter BS3. In this arrangement the temporal gate width can be controlled by the delay introduced by the two BK7 plates (P1,P2), which has a value of the order of the initial pulse duration in general, but the ratio  $I_{con}/I_{des}$  is defined by the properties of the BS3 beam splitter and corresponds to  $I_{con}/I_{des} = 0.25$ .

Below the calculated constructively and destructively interfering waveforms that result after the second beam splitter (BS2) are shown. The calculations were made with the use of Mathematica assuming a Gaussian temporal envelope, bandwidth-limited laser pulse of 36 femtoseconds duration and 804 nm central wavelength and a delay  $\delta = 36.18$  femtoseconds.

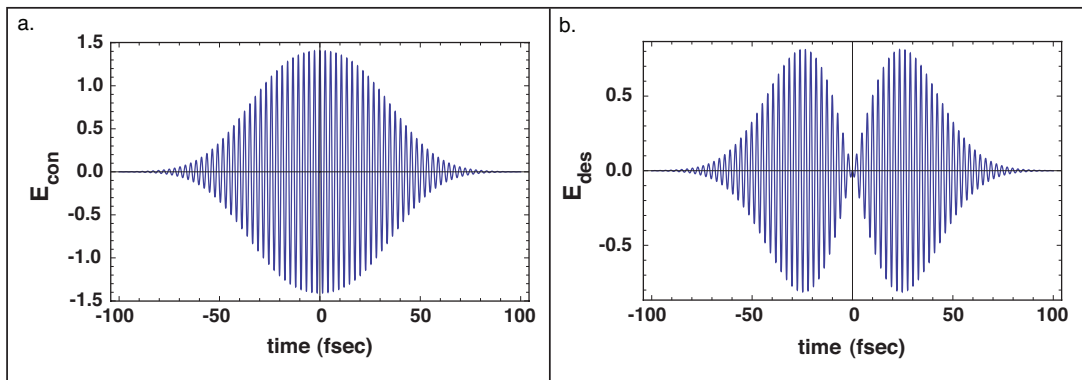


Figure 2.2: The resulting waveforms exhibiting a constructive interference maximum (a) and a destructive interference minimum (b) leaving the second beam splitter (BS2) of the double Mach-Zehnder IPG setup.

After the two pulses, of perpendicular polarization, shown above recombine in the BS3 beamsplitter exit, a laser pulse with time-dependent ellipticity is formed. The time dependent ellipticity of a laser pulse consisting of two perpendicularly polarized electric field components ( $E_x, E_y$ ) reads [22]:

$$\epsilon(t) = \tan \left[ \frac{1}{2} \sin^{-1} \left( \frac{2E_x(t)E_y(t)\sin(\Phi_x(t) - \Phi_y(t))}{|E_x(t)|^2 + |E_y(t)|^2} \right) \right] \quad (2.1)$$

where  $E_x(t)$  is the time-dependent x-direction component of the pulse electric field,  $E_y(t)$  the time-dependent y-direction component and  $\Phi_x(t), \Phi_y(t)$  the corresponding time-dependent phase components.

As already described, harmonic emission takes place when the ellipticity of the generating pulse takes values below the ellipticity threshold value  $\epsilon_{th}$ . In figure 2.3 the calculated time-dependent ellipticity of the resulting pulse is shown. The ellipticity threshold value  $\epsilon_{th_{3dH}} = 0.414$  defines the temporal gate where third-harmonic generation takes place, where in the case of high-order order harmonics the ellipticity threshold value  $\epsilon_{th_{HOH}} = 0.15$  defines a much shorter temporal gate as illustrated below.

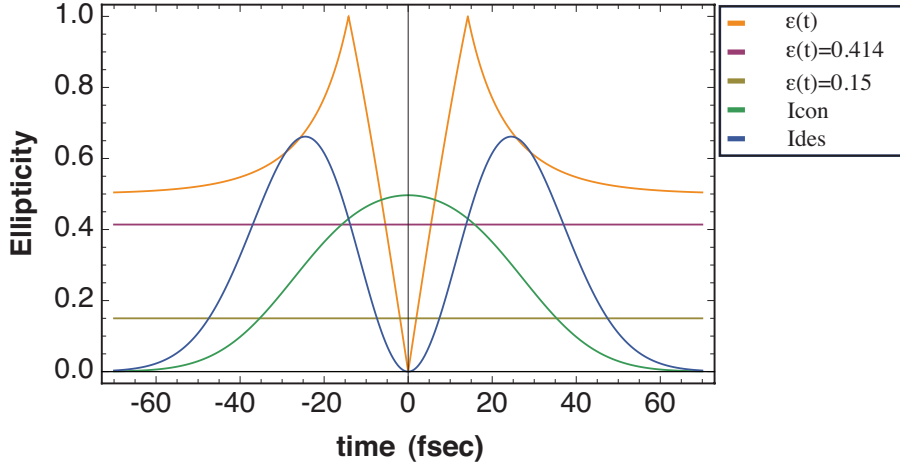


Figure 2.3: Time-dependent ellipticity of the polarization modulated pulse and ellipticity threshold for the third harmonic  $\epsilon_{th_{3dH}} = 0.414$  and for high-order harmonics  $\epsilon_{th_{HOH}} = 0.15$ .

## 2.3 Low-Order Harmonic Generation with the IPG technique

Taking advantage of the strong dependence of harmonic generation on the laser pulse ellipticity, a harmonic pulse is generated during the time interval that the pulse time-dependent ellipticity takes values below the ellipticity threshold for the specific harmonic order.

Utilizing the above described technique, intense ultrashort low-order harmonic pulses can be generated by high-power many-cycle laser systems. According to perturbation theory, the pulse duration of the generated low-order harmonics scales as  $\tau_n = \tau_L/\sqrt{n}$ , where  $n$  denotes the harmonic order and  $\tau_L$  the generating pulse duration.

By using the IPG technique, the generating pulse duration, dictated by the temporal gate width, can be made much shorter than that of the initial linearly-polarized pulse, resulting in harmonic-pulses of lower pulse duration. The pulse properties of low-order harmonics of the commonly used Ti:Sapphire lasers are very important for time-resolved photochemical studies as many organic compounds absorb in this spectral region.

In the present work the third harmonic of a Ti:S laser pulse is generated utilizing the double Mach-Zehnder IPG setup. As mentioned above the ellipticity threshold for the third harmonic corresponds to  $\epsilon_{th_{3dH}} = 0.414$  whereas for the case of the fifth harmonic the ellipticity threshold value corresponds to  $\epsilon_{th_{5th}} = 0.294$ .

As clearly illustrated in figure 2.3 the third harmonic is efficiently produced in the time interval during which the ellipticity of the driving pulse is below the  $\epsilon_{th_{3dH}} = 0.414$  value defined by the difference between the intersection points of the calculated pulse time-dependent ellipticity curve and the  $\epsilon_{th_{3dH}} = 0.414$  line. Using an initial pulse of 36 femtoseconds duration, as in our experimental conditions, and a delay value  $\delta = 36.18$  femtoseconds the above illustrated calculation predicts a temporal gate value of  $\tau_{g_{3dH}} = 10.85$  femtoseconds for the third harmonic and a temporal gate value of  $\tau_{g_{5thH}} = 7.65$  femtoseconds for the fifth harmonic. The temporal gate for high-order harmonics is defined by the ellipticity threshold value of  $\epsilon_{th_{HOH}} = 0.15$  and the calculated temporal gate corresponds approximately to one optical cycle of the generating field.

The intensity content of the temporal gate defined by the  $\epsilon_{th_{3dH}} = 0.414$  value is calculated to be  $I_{\tau_{g_{3dH}}} = 0.122I_{in}$  where  $I_{in}$  is the initial pulse intensity. For a temporal gate defined by  $\epsilon_{th_{5th}} = 0.294$  in the case of the fifth harmonic, the corresponding value is  $I_{\tau_{g_{5thH}}} = 0.119I_{in}$ . The contour plots 2.4 illustrate the results of the calculations made for the determination of the temporal gate width  $\tau_g$  as a function of the delay  $\delta$  introduced after the first beam splitter BS1 and the ratio  $I_{con}/I_{des}$  introduced by the third beam splitter BS3 and for an estimation of the ratio between the incoming pulse intensity and the temporal gate intensity content. The initial conditions used for this calculations were determined by our experimental conditions and take into account an initial Ti:S pulse of 36 fsec duration and an ellipticity threshold value of  $\epsilon_{th_{3dH}} = 0.414$ . The shaded area in the graphs indicates the parameter range  $I_{con}/I_{des} = 0.25$  and  $\delta = 36.18$  fsec, used in this experiment.

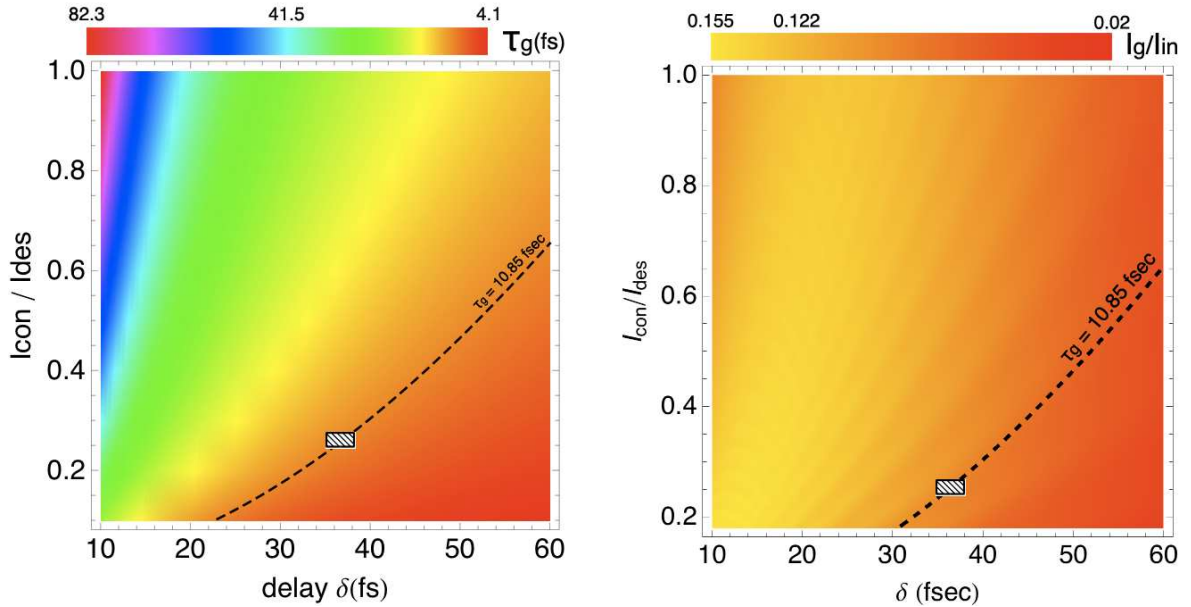


Figure 2.4: The temporal gate width  $\tau_g$  and the initial pulse - temporal gated pulse part intensity ratio are calculated as a function of the delay  $\delta$  and the  $I_{con}/I_{des}$  ratio. The shaded areas depict the experimentally used conditions for this work.

## Chapter 3

# Generation of a Third-Harmonic Pulse with the IPG technique

This chapter presents the experimental work and results of the present thesis. The objective of this work, as described above, is the generation and characterization of an intense ultrashort third-harmonic pulse utilizing the double Mach-Zehnder Interferometric Polarization Gating Technique.

An experimental setup has been built for this purpose consisting of two main parts. In the first part, high-harmonics of the fundamental laser frequency are generated and the third-harmonic is spectrally selected. The second part of the experimental setup is used for the characterization of the selected third-harmonic pulse. The experimental setup and the results obtained, will be described in detail in the following paragraphs.

### 3.1 The experimental setup

#### 3.1.1 The Ti:Sapphire Laser System

The light source used for the needs of the present work is a Chirped Pulse Amplified femtosecond Ti:Sapphire laser system. It delivers infrared laser pulses with a central wavelength of  $\lambda_L = 804$  nanometers and a spectral bandwidth of  $\Delta\lambda \approx 28$  nanometers supporting bandwidth limited laser pulses of 34 femtoseconds duration assuming a Gaussian temporal shape at 10Hz repetition rate. The pulse energy can reach the value of 170 mJoule and the beam diameter is approximately 5 centimeters.

The system consists of a commercial mode-locked Ti:S laser oscillator (Coherent Mira) pumped by an Nd:YAG (Coherent Verdi) laser providing laser pulses of about 7 nJoule per pulse at a repetition rate of 75 MHz. The pulses exiting the laser oscillator are subsequently stretched with a pair of optical gratings separating the spectral components of the pulse in time.

The chirped pulses are first amplified in a regenerative amplifier system (Amplitude Systems) pumped by an Nd:YAG (Photonics Industries) laser to reach pulse energy values of 6 mJoule. The pulses exiting the regenerative amplifier are further amplified in a two-stage multi-pass (Amplitude Systems) amplifier pumped by two Nd:YAG lasers reaching a maximum energy of 340 mJoule.

Eventually a pair of gratings is used for the compression of the pulses to a 36 femtoseconds pulse duration delivering 170 mJoules pulse energy.

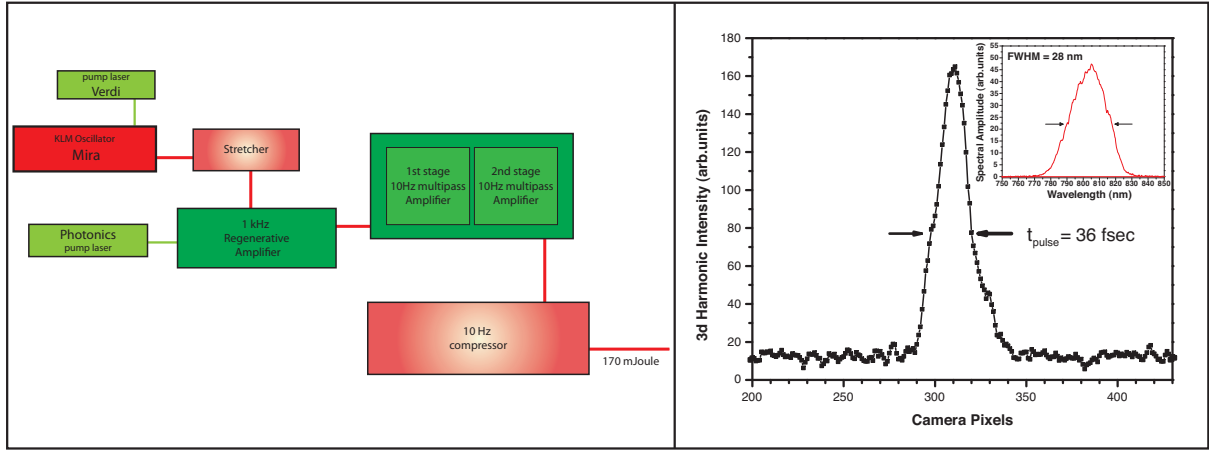


Figure 3.1: The Ti:Sapphire laser system layout is illustrated on the left side and the 3d order autocorrelation signal corresponding to a laser pulse duration of 36 femtoseconds as well as the measured spectrum of the pulse exiting the compressor part of the system on the right side.

The Ti:S laser system pulse duration has been measured with a previously developed, in the framework of the undergraduate diploma thesis of the author, single-shot third-order autocorrelation setup [23] which operates also in a high-contrast measurement scanning delay mode. This setup takes into advantage the delay introduced between the fundamental IR and the second harmonic of the fundamental laser pulse, due to the two pulse overlapping geometry on a frequency mixing BBO crystal.

The generated third harmonic signal is imaged with a UV sensitive CCD camera. The delay between the two pulses varies across the horizontal axis as a function of the horizontal position and angle between the IR and second harmonic beam on the crystal. The horizontal intensity line-out of the generated third harmonic signal, corresponds then to the third-order autocorrelation function, giving information about the initial pulse duration when a proper pulse shape is assumed. Below the single-shot third-order autocorrelation setup is illustrated as well as the produced third harmonic signal. The horizontal intensity line-out of this image is illustrated in the right part of figure 3.1, giving information about the initial pulse duration assuming a gaussian temporal shape for the Ti:S pulse.

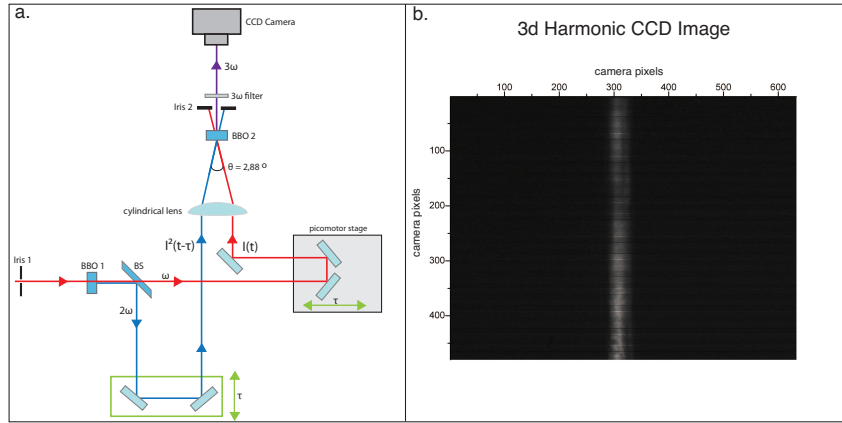


Figure 3.2: (a) The single-shot third-order autocorrelation optical setup and the corresponding (b) third harmonic image of the CCD camera.

### 3.1.2 High-harmonic generation experimental setup

The first part of the experimental setup where high harmonics of the fundamental laser pulse frequency are generated is illustrated in Fig. 3.3. The intense ellipticity modulated laser pulse, delivered from the double Mach-Zehnder IPG setup, is focused in the interior of a vacuum chamber, with the use of a 1 meter focal length lens (L), just under the tip of a pulsed gas nozzle (PJet) that provides the noble gas target, which in our case is Argon gas, for the generation of high-harmonics.

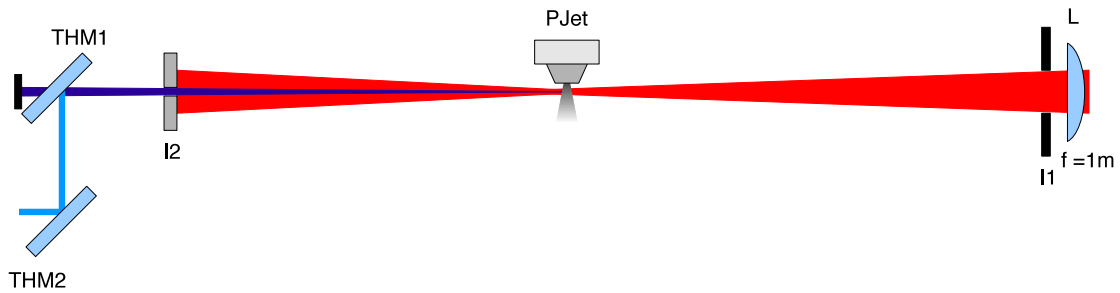


Figure 3.3: High-harmonic generation experimental setup. The third-harmonic is spectrally selected with the THM1 and THM2 mirrors and directed to the characterization experimental setup.

The vacuum chamber is in general divided in the high-harmonic production part and the third harmonic characterization part which will be described in detail in the next paragraph. The generating beam waist is adjusted with use of an iris (I1) just after the focusing lens, having 1 cm diameter, as well as the jet position with respect to the focal spot, in order to achieve good phase-matching conditions for the generation of the third-harmonic that is here of interest.

An oil-sealed rotary vacuum pump keeps the ambient pressure in the harmonic generation part of the vacuum chamber under  $10^{-3}$  mbar, reaching a highest value of  $7.2 \times 10^{-2}$  mbar during gas jet operation.

The pulsed gas jet consists of a stainless steel casing, loaded with Argon at a pressure of 2.5 bar, ending to an adjustable nozzle which is sealed from the vacuum chamber with a rubber poppet. The rubber poppet is actuated by a circular piezoelectric crystal, providing a noble gas leak in the vacuum chamber in a pulsed mode. This is achieved by providing an electric pulse of controlled amplitude and width to the piezoelectric crystal. The operation of the pulsed gas jet is triggered by one of the laser amplification system Pockels-cells with an appropriate time delay introduced by a Stanford Research Systems delay generator, so that the generating pulse and the gas release are synchronized.

As mentioned in the first chapter of this thesis, the generated harmonics propagate in the same direction as the generating pulse exhibiting in general a much smaller angular spread that depends on harmonic order. A circular aperture (I2) is used after the harmonic-generation area blocking a large portion of the IR beam, letting the harmonic beam to come through and allowing also for differential pumping between the high-harmonic production area and the characterization area of the experimental setup.

The third harmonic is spectrally selected from the harmonic beam with the use of two mirrors (THM1, THM2) that reflect the third harmonic and transmit the rest of the incident radiation.

### 3.1.3 Third-harmonic characterization experimental setup

The experimental setup where the characterization of the third harmonic takes place, situated in a vacuum chamber is shown schematically in Fig. 3.4.

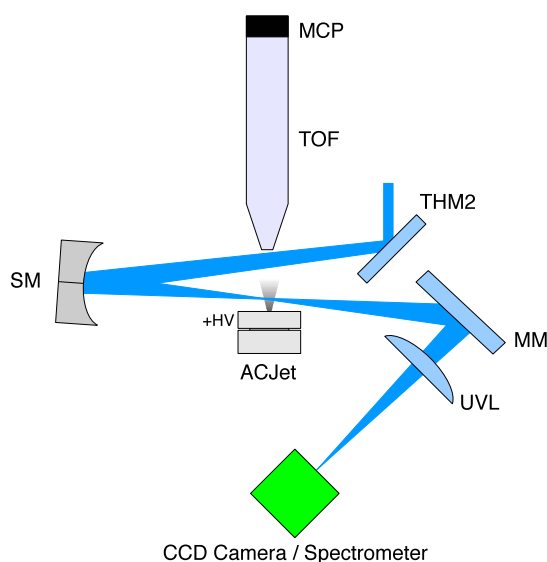


Figure 3.4: The third-harmonic pulse characterization part of the experimental setup.

The third harmonic beam reflected by the THM2 mirror is directed in the central part of a spherical mirror, of 5 centimeters focal length, cut into two-halves (SM) having a 70% reflectivity value for the third-harmonic wavelength, that brings the two parts of the bisected third-harmonic pulse into a common focus in front of the tip of a pulsed magnetic jet (ACJet) which is situated in front of a time-of-flight spectrometer tube opening.

The two split-mirror parts are mounted in two separate translation stages that are controlled by two New Focus Vacuum Picomotor actuators with a less than 30nm step-size specification corresponding to 0.2 femtoseconds time resolution. In this way a controllable delay is introduced between the two parts of the focal spot, originating from the two separate parts of the focusing mirror. The third harmonic-beam is focused at a slight angle in front of the pulsed magnetic jet tip due to space limitations of the current vacuum chamber.

The magnetic gas jet is in a floating ground scheme so that a homogeneous electric field for the acceleration of generated ions is formed between the circular metal plate surrounding the jet nozzle and a copper grid at the time-of-flight tube (TOF) opening that is earth grounded with the vacuum chamber. The synchronization of the magnetic jet with the third-harmonic pulse is achieved in the same way as in the case of the high-harmonic generation jet.

By applying a positive high-voltage of the order of 1000 Volts on the magnetic jet metal plate, a homogeneous electric field is formed that accelerates the ions produced, by the interaction of the focused third-harmonic pulse with the gas-phase target provided by the pulsed magnetic jet, towards the field-free time-of-flight spectrometer tube.

The accelerated ions reach subsequently a Micro-Channel Plate (MCP) detector and the ion time-of flight spectrum is observed with the use of a Tektronix Digital Oscilloscope.

After leaving the focus position the third-harmonic beam is reflected by a metal mirror (MM) outside the vacuum chamber and focused by a  $f = 10\text{cm}$  UV lens (UVL) in the plane of the sensor of a Cohu 4810 CCD Camera imaging the split-mirror focal spot. The protective glass in the front of the CCD sensor has been removed and the camera is UV sensitive. An appropriate filter transmits only the third harmonic that reaches the CCD sensor.

Alternatively the CCD camera can be replaced by the optical fiber probe of an Ocean Optics HR4000CG UV-NIR Spectrometer, with a spectral working range of 193-1050 nanometers, used for the spectral characterization of the third-harmonic pulse.

The vacuum chamber where the characterization of the third harmonic takes place, communicates with the high-harmonic generation chamber through the aperture I2 as described above. It is pumped down to  $8 \times 10^{-6}$  mbar with the use of two 150 l/sec turbo-molecular pumps supported by two additional rotary pumps. The first turbo-molecular pump is located under the magnetic jet nozzle and the second pumps the time-of-flight tube in order to achieve high vacuum conditions in this area.

The Micro-Chanel Plate (MCP) detector is a commercial, resistance matched, detector with two MCP plates in a chevron arrangement with an operating voltage of 1500-1800 Volts.

### 3.2 Spectral Characterization of the Third-Harmonic Pulse

As described above the third-harmonic pulse exits the vacuum chamber and is focused with a 10cm focal length UV lens. By placing an optical fiber probe at the focal spot, the third-harmonic spectrum is measured with the Ocean Optics HR4000CG UV-NIR Spectrometer.

The third-harmonic spectrum has been measured for two different generation conditions. First the linearly polarized Ti:S laser pulse is used to generate the third harmonic, where in the second case the ellipticity modulated pulse exiting the double Mach-Zehnder IPG setup is used. In both cases a generating beam diameter of 1cm, adjusted with the I1 iris, is used and Argon as a generating medium. After optimizing the experimental conditions for both cases the third-harmonic pulse spectrum is recorded with the SpectraSuite software that accompanies the spectrometer. The spectra obtained for both cases are shown below.

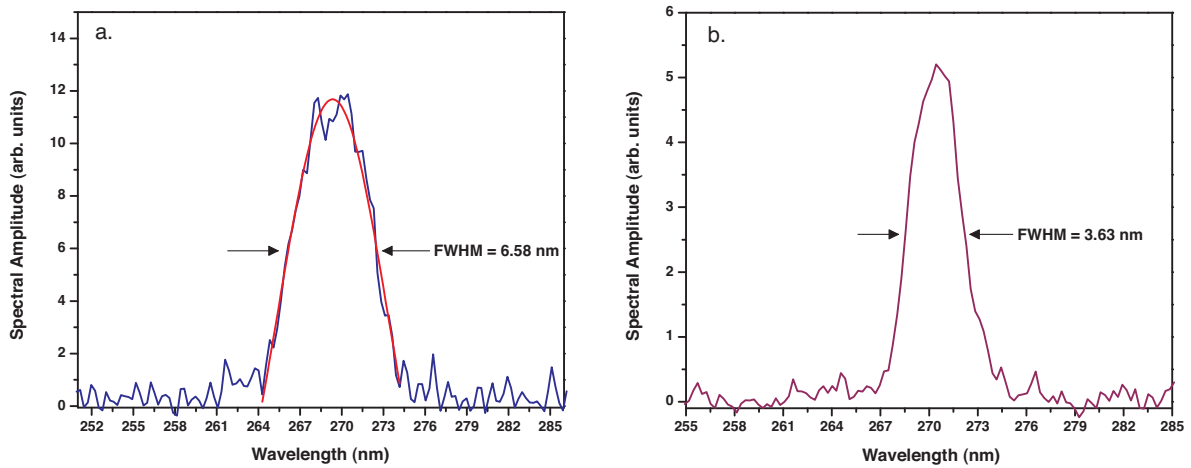


Figure 3.5: Third-harmonic spectra obtained (a) for an ellipticity modulated generating Ti:S pulse exiting the double Mach-Zehnder IPG setup and (b) for a linearly polarized generating pulse.

As expected, according to the previous analysis the spectrum of the third-harmonic pulse generated from the double Mach-Zehnder IPG ellipticity modulated pulse exhibits a broader spectrum than in the case when a linearly polarized generating pulse is used, corresponding to a smaller third-harmonic pulse duration according to equation 1.1. Here the generated bandwidth from the ellipticity modulated Ti:S pulse is much broader than that generated by the linearly-polarized Ti:S pulse and supports the formation of a gauss-shaped bandwidth-limited third harmonic pulse of approximately 16.16 femtoseconds duration. The above spectra correspond, according to the above analysis to a generating IR pulse of 50 fs duration. Variation of the generating pulse duration is expected if the laser systems compressor gratings are not in the distance that gives a bandwidth limited pulse. In general the distance between the two gratings is controlled with a micrometric translation stage where the one grating is positioned.

In a previous work [23] it was shown experimentally supported by theoretical calculations that a very small displacement of this grating can alter significantly the laser pulse duration delivered by the laser system. Furthermore, the IPG technique allows precise control of the parameters that produce the time-dependent ellipticity modulation of the generating pulse and gives the expected results even for a slightly longer generating pulse. For the optimization of the generated third-harmonic pulse duration the previously developed single-shot third-order autocorrelation setup can be used online.

The broad bandwidth generated with use of the IPG technique supports the generation of a shorter third-harmonic pulse. This spectral measurement does not provide unfortunately information about the corresponding third-harmonic pulse duration but only for the minimum duration that can be achieved as dictated by equation 1.1, as we do not obtain information about the spectral phase distribution. For the temporal characterization of the pulse the second-order intensity volume autocorrelation method [15],[24],[25] will be employed, which will be described in detail in the following section.

### 3.3 Temporal Characterization of the Third-Harmonic Pulse

#### 3.3.1 The 2<sup>nd</sup> Order Intensity Volume Autocorrelation Technique

For the temporal characterization of the third-harmonic pulse the second-order intensity volume autocorrelation technique [24],[25] will be employed. This technique is an extension of the commonly used, in femtosecond pulse metrology, second-order autocorrelation technique.

For the implementation of this method a second-order nonlinear process is needed in order to produce the second-order autocorrelation trace that determines directly the third-harmonic pulse duration. In our case the second-order autocorrelation signal is provided by the two-photon resonantly-enhanced ionization of toluene ( $C_7H_8$ ) [26], that results by the superposition of the two parts of the third-harmonic pulse at the split-mirror focus interacting with the toluene vapor provided by the magnetic gas jet in the characterization area.

By translating the one part of the split mirror with use of the Picomotor actuator and recording ion signal produced by two-photon ionization, the second-order autocorrelation trace can be obtained as a function of the delay between the two third-harmonic pulse parts  $\tau = 2\delta x/c$  where  $\delta x$  denotes the displacement between the two split-mirror parts.

The split-mirror focal spot has an Airy pattern shape for zero delay between the two parts of the pulse and exhibits a complicated pattern as a function of their relative displacement becoming a well divided two-spot Airy pattern when the displacement is a multiple of half-wavelength of the focused pulse [24]. This double-spot can be used in order to align the incoming pulse to the central part of the split mirror and in order to equally divide the third-harmonic pulse intensity, in the two split-mirror parts, which is important for this measurement signal contrast enhancement.



Figure 3.6: The calculated split-mirror focus for (left) zero delay between the two pulse parts and for (right)  $\tau = \lambda/2$  delay. Taken from [24].

In the commonly used in femtosecond metrology, second-order autocorrelation, the nonlinear medium is a crystal or a non-linear photodiode and the autocorrelation signal is produced as a variation of the intensity reaching the detector as a function of the delay between the two parts of the pulse. In the second-order intensity volume autocorrelation however, the delay between the two pulse parts results in a spatial redistribution of the energy inside the focal volume. The non-linearity that produces the measured signal in this case ensures the signal modulation and in general the signal contrast is reduced in comparison to the conventional second-order autocorrelation technique. It can be easily realized that the signal produced for example for a delay of half wave displacement between the two split-mirror parts the signal is proportional to  $(I_{3dh}/2)^2 + (I_{3dh}/2)^2 = I_{3dh}^2/2$  in contrast to the zero delay case where the measured signal is proportional to  $I_{3dh}^2$ . In general dividing the pulse intensity unequally between the two split-mirror parts or having a fringe pattern at zero delay can significantly lower the signal contrast according to the above analysis.

The applicability of this method was investigated for the case of our experimental conditions. In the present experiment the generating beam waist is adjusted for efficient third-harmonic generation and the optimization of the third-harmonic signal is achieved with the help of the Ocean Optics spectrometer. The entrance iris I1 is adjusted, having 1cm diameter for maximum third-harmonic signal.

This diameter delivers a 4,5 mJoule pulse and for a conversion efficiency value for the third-harmonic of  $10^{-3}$  [27], we estimate that the third-harmonic pulse energy corresponds to  $E_{3dh} = 4.5\mu J$ . The two mirrors that select the third-harmonic pulse (THM1,THM2) have a reflection coefficient of 0.9 and the focusing split-mirror 0.7. The third-harmonic pulse energy after the split mirror is estimated to have an energy content of  $E_{3dh} = 2.55\mu J$ .

According to perturbation theory and assuming a gaussian intensity distribution, the third harmonic beam diameter as compared with that of the infrared generating beam should be  $D_{3dh} = D_{IR}/\sqrt{3} = 0.57cm$  and the pulse duration  $\tau_{3dh} = \tau_{IR}/\sqrt{3} = 20.8$  fsec for a  $\tau_{IR} = 36$ fsec infrared pulse duration. Using these values the intensity of the third-harmonic pulse at the focal spot of the split-mirror is estimated to be  $I_{3dh} \approx 1.65 \times 10^{15} W/cm^2$ . In this case we have sufficient intensity to induce the second-order non-linear process needed to produce and the second-order intensity volume autocorrelation signal for the pulse duration measurement of the third-harmonic pulse.

### 3.3.2 The Non-Linear Medium

The toluene molecule ( $C_7H_8$ ) in the gas-phase, serves in our case as the nonlinear detector having an ionization potential of  $8.828 \pm 0.001$  eV [28] which is less than the third-harmonic two-photon energy of 9.2 eV ( $2 \times \hbar\omega_{3dh} = 9.2eV$ ).

As mentioned above the third-harmonic pulse is focused at the tip of a magnetic pulsed gas jet. Toluene vapor is delivered in a pulsed mode in the vacuum chamber, synchronized with the third-harmonic pulse with the laser system amplifier Pockels-cell signal and a Stanford Research Systems delay generator.

The tip of the jet is aligned with a time-of-flight mass spectrometer axis and perpendicular to the third-harmonic pulse propagation direction as illustrated in figure 3.4. A homogeneous electric field between the magnetic jet cylindrical head and the copper grid at the time-of-flight tube entrance accelerates the positively charged toluene ions towards the TOF entrance. After entering the field-free tube, the ions reach the micro-channel plate detector and the time-of-flight mass spectrum is obtained with a Tektronix Digital Oscilloscope as described above.

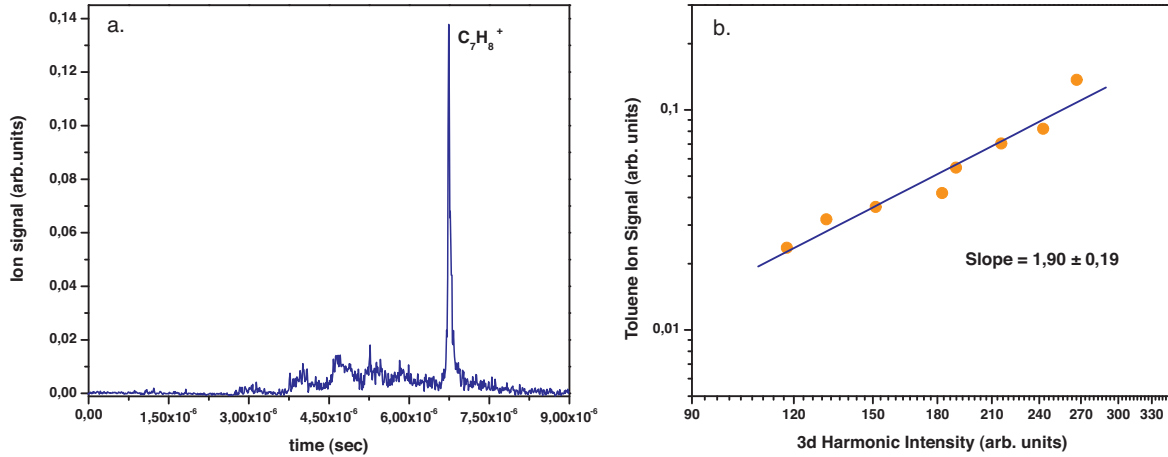


Figure 3.7: (a.) The two-photon ionized toluene time-of-flight ion mass spectrum and (b.) the toluene ion signal as a function of the third-harmonic pulse intensity in logarithmic scale. The slope of the log-log plot equals  $1.9 \pm 0.19$  and provides clear experimental evidence of the two-photon ionization of toluene which can be used as the second-order nonlinear medium needed for performing the second-order volume autocorrelation measurement of the third-harmonic pulse.

The third-harmonic pulse beam after leaving the spherical split-mirror focus is focused again at the tip of a UV-NIR Ocean Optics Spectrometer optical fiber probe after exiting the characterization vacuum-chamber using a 10cm focal length UV lens. This arrangement permits the simultaneous ion signal and third-harmonic pulse spectral intensity data acquisition. The third-harmonic pulse spectral intensity data are obtained with use of the UV-NIR Ocean Optics Spectrometer SpectraSuite software.

By using a beam-stop of 1 cm diameter an annular-shaped beam is formed and used to generate high-harmonics of the fundamental laser frequency. The infrared radiation content in the characterization area is eliminated in this way. Measurements of the toluene ion signal as a function of the third-harmonic pulse intensity have been performed for the investigation of the nonlinear properties of the medium. By varying the harmonic-production jet electric pulse amplitude we are able to adjust the third-harmonic pulse intensity and measure the dependence of the toluene ion signal as a function of the third-harmonic pulse intensity.

The toluene ion signal exhibits a quadratic dependence on the third-harmonic pulse intensity as shown in figure 3.7b and therefore clear evidence of a two-photon ionization process is provided. A typical toluene time-of-flight mass spectrum and the toluene ion signal intensity dependence in log-log plot are shown above. Since the second-order nonlinear process needed for the second-order autocorrelation signal has been experimentally verified, imaging of the split-mirror focal spot is essential giving the ability to precisely align the third-harmonic pulse in the center of the split-mirror and equally divide the third harmonic pulse intensity content in the two spherical mirror parts.

### 3.3.3 Split-Mirror Focal Spot

The first step towards performing the second order intensity volume autocorrelation measurement of the third-harmonic pulse is imaging the split-mirror focal spot. This is very important, because it allows to spatially overlap the two resulting focal spots from the two parts of the split-mirror in a controlled manner and also to be able to reach the temporal overlap position by observing the interference pattern of the spatially overlapping spots according to the above analysis.

The split-mirror focal spot is imaged with the use of a UV lens outside the vacuum chamber on a UV sensitive CCD camera sensor placed at the focal plane of the resulting lens system. The tilting of the two split-mirror parts is controlled by the split-mirror mount tilting screws via vacuum feedthrough controls.

The two resulting focal spot parts were imaged and made to spatially overlap in the best possible way, given the fact that the feedthrough screw-based tilting system does not provide precise control. The focal spot shows astigmatism due to the angle of incidence and reflection of the third harmonic pulse by the split-mirror. Astigmatism is observed even after optimizing the alignment of the third-harmonic beam in the characterization optical setup since space limitations of the used vacuum chamber do not allow for smaller angles to be used.

In our case the third-harmonic beam passes under the time-of-flight tube entrance hitting the split mirror at a lower position from the mirror center. The angle between the incident and the reflected third-harmonic beam is estimated in the best possible alignment conditions for the current experimental setup to be  $\theta = 10^\circ \pm 2^\circ$ . A different vacuum chamber would allow nearly collinear beam alignment conditions and would be therefore possible to eliminate astigmatism in the focal spot.

A ray-tracing investigation for the split-mirror focal spot properties, tailored to our experimental conditions has been performed with the Mathematica ray-tracing package Optica with the help of Manolis Skantzakis. In this calculation we produce a third harmonic beam at a distance from the spherical mirror equal to the distance from the high-harmonic production jet to the spherical split-mirror, as a cone of rays defining a circular beam. The next step is the calculation of the resulting focal spot under different beam alignment conditions. First we calculate the resulting focal spot shape in the case of a third-harmonic beam incident at the central part of the focusing mirror as a function of the angle of incidence of the 3d harmonic beam on the spherical mirror.

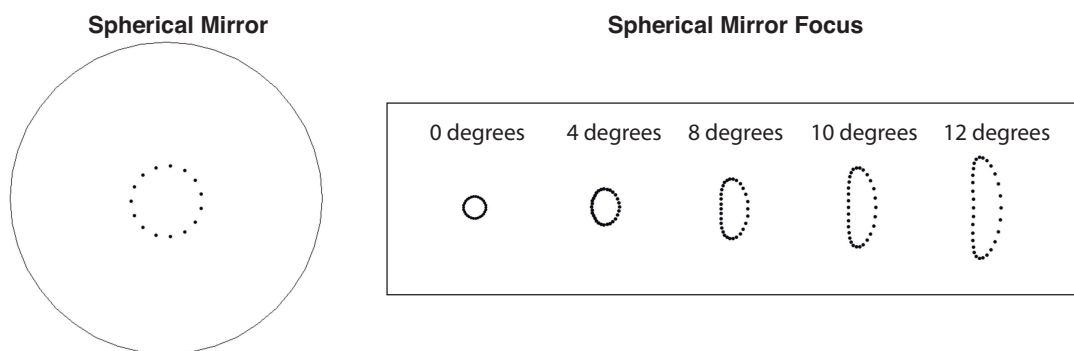


Figure 3.8: Ray-tracing calculation results for the split-mirror focal spot shape when the third-harmonic beam is incident to the central part of the spherical mirror as a function of the angle of incidence.

It is evident, that as the angle of incidence is increased the resulting focal spot becomes more astigmatic. However for a small angle, up to 4 degrees the resulting focal spot is not significantly distorted with respect to the 0 degree shape. In the second case, which immitates our experimental conditions, the third-harmonic beam is incident at a lower position from the central part of the spherical mirror as illustrated below.

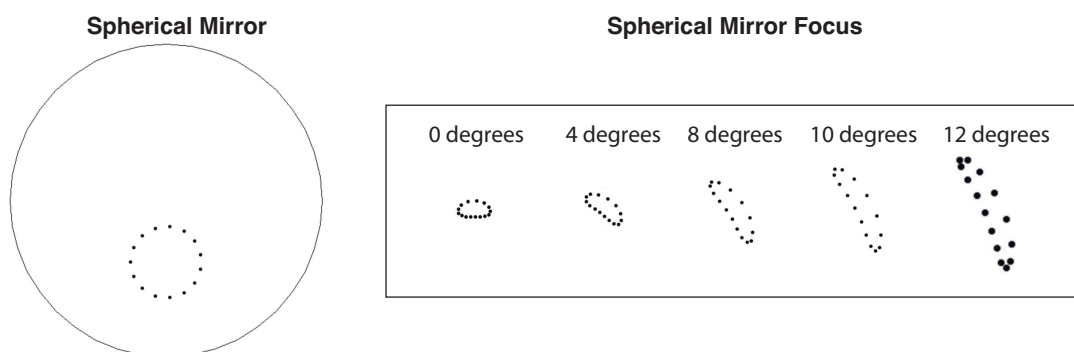


Figure 3.9: Ray-tracing calculation results for the split-mirror focal spot shape when the third-harmonic beam is incident lower than the central part of the spherical mirror as a function of the angle of incidence.

In this case the resulting focal spot exhibits astigmatism even at a collinear geometry. In both cases the calculations consider the third-harmonic beam wave-vector parallel to the unit vector perpendicular to the center of the spherical mirror surface. In the case of our experimental conditions and for an angle of  $\theta = 10^\circ \pm 2^\circ$  the focal spot is astigmatic and as a result the above mentioned splitting of the Airy disk is impossible to be observed. Instead a fringe pattern is expected due to the particular third-harmonic beam geometry.

The imaged focal spot with use of the UV sensitive CCD camera is shown below. After the two parts originating from the two split-mirror sides are made to overlap, the Picomotor actuated translation stage is used for achieving temporal overlap between the two parts. At the zero-delay position interference fringes are observed as expected. The image of the two astigmatic spots overlapping in space and time is shown below.

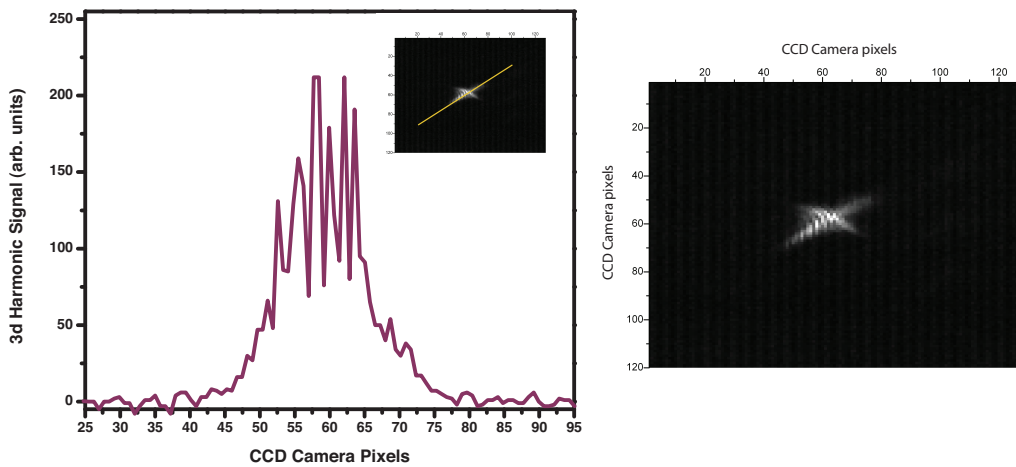


Figure 3.10: Imaging of the split-mirror focal spot when the two spots overlap in space and time. The two spots exhibit astigmatism due to the limiting experimental optical arrangement. On the left part the intensity line-out is illustrated where interference fringes are observed in perfect temporal overlap (zero delay between the two spots).

The observed multi-peak fringe pattern is expected to significantly lower the contrast of the measured signal that results from the two-photon ionization of toluene. This is also evident in the following section where the second-order intensity volume autocorrelation trace is obtained. Replacement of the used vacuum chamber would allow for collinear alignment geometry, eliminating astigmatism and giving the ability to divide equally the third-harmonic pulse intensity in the two split-mirror parts.

### 3.3.4 $2^{nd}$ Order Intensity Volume Autocorrelation Measurement of the Third-Harmonic Pulse

In this part the data acquisition process and results of the second-order volume autocorrelation trace will be described. The first step towards the trace acquisition is the alignment of the

split-mirror focal spot in a way that the two third-harmonic pulse parts overlap in space and time.

The spatial overlap is achieved by the alignment of the third-harmonic beam in the central part of the split-mirror with use of the vacuum-feedthrough screws that control the mirror THM1 tilting screws and the help of the split-mirror focal spot imaging system which allows for real-time monitoring of the alignment process. By using the vacuum-feedthrough split-mirror tilting screws the third-harmonic pulse is focused at the tip of the pulsed toluene gas jet.

For the temporal overlap of the two parts of the third-harmonic pulse the New Focus Picomotor software is used for the translation the one split-mirror part until the fringe pattern is observed and optimized.

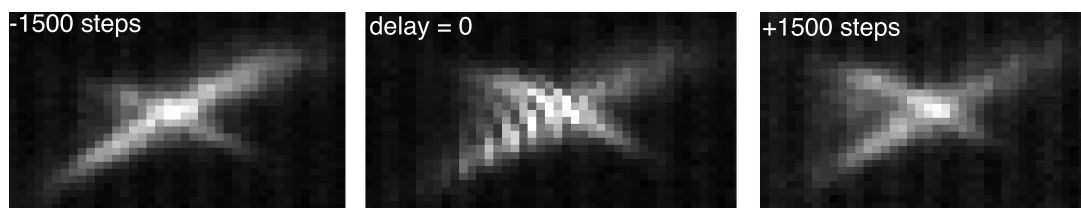


Figure 3.11: Imaging of the split-mirror focal spot in the zero-delay position and for  $\pm 1500$  picomotor steps of displacement positions. Before and after the zero delay position the fringe pattern disappears.

When spatial and temporal overlap has been achieved, then this position is set as position zero in the picomotor software interface and the motor is then used for reaching a position of the translation stage where the two parts have a considerable temporal delay. For this purpose the translation stage is moved backwards by the picomotor actuator typically 2000-3000 steps away from the zero delay position. For a step size of 30 nm, that is the upper limit of the picomotor step size specification for the translation speed we use, each step corresponds to 200 attoseconds delay.

By scanning a number of  $\pm 3000$  steps around the zero delay position we scan an equivalent delay range of  $\pm 600$  femtoseconds. This temporal range is sufficient since we expect a pulse duration of the order of 10 to 100 femtoseconds at most. Also scans of the order of  $\pm 5000$  steps have been performed in order to investigate the general behavior of the traces.

A specially developed Labview software that communicates with the Tectronix Oscilloscope is used to place a data collecting gate around the peak of interest, here the two-photon ionized toluene ion peak, and record the integrated peak values as a function of time in our case. Simultaneously the picomotor controlling software moves the translation stage at a 2 steps per second speed from a maximum negative temporal delay towards the zero delay position and reaching a positive maximum temporal delay value as described above. The two-photon ionized toluene ion peak integral is recorded as a function of this delay at the same time. The small picomotor scanning speed allows for an averaging of 5-10 shots per data point improving the experimental statistics.

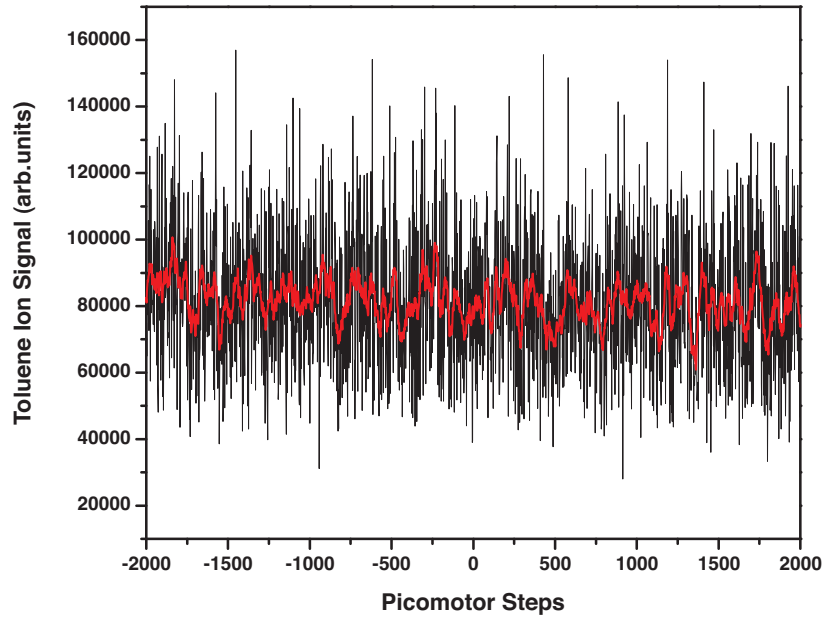


Figure 3.12: The 2<sup>nd</sup> Order Intensity Volume Autocorrelation trace. The contrast of the measured signal is reduced significantly due to the focusing geometry in our case. The observed fringe pattern at the zero delay position explains the lack of measurable modulation in the toluene ion signal.

The third-harmonic beam geometry, as described in the previous section, produces an astigmatic focal spot exhibiting a fringe pattern at zero-delay that significantly lowers the two-photon ionized toluene ion signal contrast. As clearly illustrated above, no measurable modulation of the ion signal can be detected under this focusing geometry conditions.

Under the particular conditions and after excessive efforts in the optimization of the focusing geometry using the particular space-limiting vacuum chamber the measurement of a considerable modulation of the toluene ion signal is impossible and thus we cannot reach safe conclusions about the third-harmonic pulse duration.

However an improvement of the focusing conditions by replacement of certain parts of the experimental setup will allow the temporal characterization of the third-order harmonic pulse, providing valuable information about the low-order harmonic generation with the use of the IPG technique.

### 3.4 Conclusions - Future Plans

In the frame of this Master thesis, the generation of low-order harmonics of the fundamental Ti:S laser pulse frequency has been investigated. In the first part, the ellipticity modulated laser pulse properties that directly define the low-order harmonic pulse generation conditions were calculated by a personally developed code using Mathematica. This code is used for the calculation of the time-dependent ellipticity of the pulse exiting the double Mach-Zehnder IPG arrangement and provides information about the temporal gate width formed, the temporal gate intensity content and properties, defined by the initial laser pulse properties and the desired ellipticity threshold value.

In the second part an experimental setup was built for the generation and characterization of low-order harmonic pulses using the interferometric polarization gating technique. A broad bandwidth third-harmonic pulse was generated with use of the IPG technique and the pulse spectral width has been compared with the case of a linearly-polarized generating pulse. In full agreement with our calculations the third-harmonic pulse bandwidth is significantly increased when an ellipticity-modulated generating laser pulse is used, supporting a third-harmonic pulse of shorter duration and promising for even shorter pulse duration for the low-order harmonics according to our calculation results.

For the determination of the third-harmonic pulse duration an experimental setup allowing the performance of the  $2^{nd}$  order intensity volume autocorrelation measurements was built and thoroughly characterized. The toluene ion signal dependence on the third-harmonic pulse intensity scales quadratically, denoting a two-photon ionization process that is needed for performing second-order intensity volume autocorrelation measurement of the pulse. The limiting vacuum chamber space and coarse beam tilting controls did not allow the measurement of the pulse in the time frame that was available for the completion of this Master thesis.

However valuable conclusions were drawn for future improvement of the experimental apparatus. More specifically, the major limitation for this measurement results from the spherical bisected focusing mirror focusing geometry. As shown experimentally and supported by the third-harmonic ray-tracing investigation the third-harmonic focal spot shows considerable astigmatism for an angle of incidence higher than 4 degrees. The focal spot astigmatism lowers the produced ion signal contrast to an extent that no signal modulation can be observed and therefore no safe conclusion about the third-harmonic pulse duration can be drawn.

The improvement of the particular experimental setup includes the replacement of the third-harmonic characterization vacuum chamber, so that enough space will be provided for near-collinear beam focusing conditions. This will significantly decrease the focal spot astigmatism and increase the ion signal contrast. Furthermore, replacement of the vacuum feedthrough screw tilting controls with stepper-motors will allow for the precise control of the third-harmonic beam alignment and will aid the optimization of the ion signal contrast.

## Appendix A

# Mathematica Code for the Ellipticity Modulated Pulse Calculations

```
Initial Parameters ;  
Centralwavelength = 804 (*nm*);  
omega = (2 * 3.141592653589 * 3 * 10 ^ 17) /  
  (Centralwavelength * 10 ^ 15); (*1/fs*)  
FWHM = 36 (*fs*);  
(*Initial Pulse Duration (Intensity Profile)*)  
T = (2 * 3.141592653589) / omega ;  
delta = 27 * (T / 2);  
(*Delay introduced between the 2 pulses ->  
  Multiple of T/2 for interference*)  
delred = delta / 2;  
Needs["PlotLegends`"]
```

*Ellipticity Threshold Calculation ;*

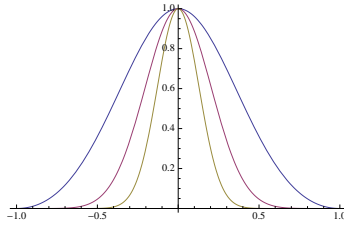
```
(*Solve [ ( (1 - epsilon^2) / (1 + epsilon^2) )^(q-1) == Iq, epsilon ] ; *)  
  
(* { { epsilon -> - ( sqrt(1 - Iq^(1/(1-q))) / sqrt(1 + Iq^(1/(1-q))) },  
  { epsilon -> ( sqrt(1 - Iq^(1/(1-q))) / sqrt(1 + Iq^(1/(1-q))) } } ; *)  
  
epsilon[q_, Iq_] := ( sqrt(1 - Iq^(1/(1-q))) / sqrt(1 + Iq^(1/(1-q))) );  
  
Intensity[q_, epsilon_] := ( (1 - epsilon^2) / (1 + epsilon^2) )^(q-1) ;
```

```
epsilon[3, 0.5]  
0.414214
```

```

Plot[{ε[q, 0.5], 0.15}, {q, 3, 16},
  AxesOrigin → {2.5, 0},
  Ticks →
    {{0, 3, 5, 7, 9, 11, 13, 15, 17, 19, 21, 23,
      25, 27, 29, 31, 33, 35},
     {0.05, 0.1, 0.15, 0.2, 0.25, 0.3, 0.35, 0.414}},
  AxesLabel → {"q", "Iq"}, PlotRange → {All, All}]
Plot[{Intensity[3, ε], Intensity[7, ε],
  Intensity[16, ε]}, {ε, -1, 1}]

```



Beamsplitter #1;

```

Plot[
  Re[Exp[-(t)^2 / ( (2/√2 FWHM) / (2√Log[2]) )^2 ] Exp[i * (omega * t) ]],
  {t, -130, 130}, PlotRange → {All, All},
  AxesLabel → {"time(fs)", "E.Field"},
  BaseStyle → {FontFamily → "Times", FontSize → 16},
  PlotPoints → 150]

Etrans1[t_] := Exp[-(t)^2 / ( (2/√2 FWHM) / (2√Log[2]) )^2 ] *
  Exp[i * (omega * t)];

Erefl1[t_] := Exp[-(t)^2 / ( (2/√2 FWHM) / (2√Log[2]) )^2 ] *
  Exp[i * ((omega * t) + Pi)];
(*Plot[{Re[Etrans1[t]], Re[Erefl1[t]]},
  {t, -130, 130}, PlotRange → {All, All},
  AxesLabel → {"time(fs)", "E.Field"},
  BaseStyle → {FontFamily → "Times", FontSize → 16},
  PlotPoints → 150] *)

```

Beamsplitter #2;

```

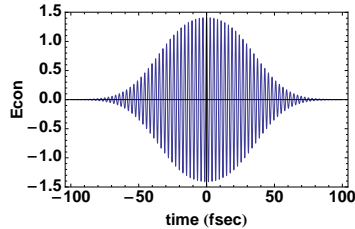
Erefl2[t_] :=
  Exp[-((t + delred))^2 / ( (2/√2 FWHM) / (2√Log[2]) )^2 ] *
  Exp[i * ((omega * (t + δ)) + Pi)] +
  Exp[-((t - delred))^2 / ( (2/√2 FWHM) / (2√Log[2]) )^2 ] *
  Exp[i * (omega * (t))];
Etrans2[t_] :=
  Exp[-((t - delred))^2 / ( (2/√2 FWHM) / (2√Log[2]) )^2 ] *
  Exp[i * (omega * (t - (δ / 2)))] +
  Exp[-((t + delred))^2 / ( (2/√2 FWHM) / (2√Log[2]) )^2 ] *
  Exp[i * (omega * (t + (δ / 2)))]];

```

```

Plot[Re[Erefl2[t]], {t, -100, 100},
  PlotRange -> {All, All},
  BaseStyle -> {FontFamily -> "Helvetica",
    FontSize -> 14}, PlotPoints -> 300,
  FrameLabel -> {"time (fsec)", "Econ"},
  PlotStyle -> Thickness[0.003],
  LabelStyle -> Directive[Bold, FontSize -> 14,
    FontFamily -> "Helvetica"], Frame -> True]
Export["ConsField.eps", %]

```

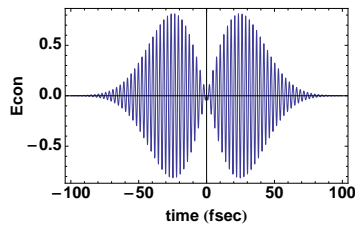


ConsField.eps

```

Plot[Re[Etrans2[t]], {t, -100, 100},
  PlotRange -> {All, All},
  BaseStyle -> {FontFamily -> "Helvetica",
    FontSize -> 14}, PlotPoints -> 300,
  FrameLabel -> {"time (fsec)", "Econ"},
  PlotStyle -> Thickness[0.003],
  LabelStyle -> Directive[Bold, FontSize -> 14,
    FontFamily -> "Helvetica"], Frame -> True]
Export["DesField.eps", %]

```



DesField.eps

*Beamsplitter #3:*

(\*After the 3d BS the 2 components are  
combined to a polarization-  
modulated pulse where the constructive  
part is the 1/4 in Intensity  $0.5^2=0.25$ \*)

```

Ex[t_] := 0.5 Erefl2[t]
Ey[t_] := Etrans2[t]
φx[t_] := ArcTan[(Im[Ex[t]] / Re[Ex[t]])]
φy[t_] := ArcTan[(Im[Ey[t]] / Re[Ey[t]])]

```

```

ε[t_] :=
  Tan[
    0.5
    ArcSin[
      (2 * Abs[Ex[t]] * Abs[Ey[t]] *
        Sin[(φx[t] - φy[t])]) /
      ((Abs[Ex[t]] ^ 2 + (Abs[Ey[t]] ^ 2))]
    ]

```

```

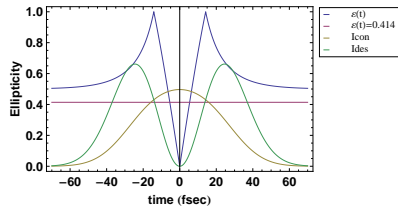
Plot[{Re[Ex[t]], Re[Ey[t]]}, {t, -5, 5},
  PlotRange -> {All, All},
  AxesLabel -> {"time (fs)", "E. Fields"},
  BaseStyle -> {FontFamily -> "Times", FontSize -> 16},
  PlotPoints -> 100]

```

```

Plot[{Abs[ $\epsilon$ [t]], 0.414, Abs[Ex[t]]^2,
Abs[Ey[t]]^2}, {t, -70, 70},
PlotRange -> {All, All},
BaseStyle -> {FontFamily -> "Helvetica",
FontSize -> 14}, PlotPoints -> 300,
FrameLabel -> {"time (fsec)", "Ellipticity"},
PlotStyle -> Thickness[0.003],
LabelStyle -> Directive[Bold, FontSize -> 11,
FontFamily -> "Helvetica"], Frame -> True,
PlotLegend -> {" $\epsilon$ (t)", " $\epsilon$ (t)=0.414", "Icon",
"Ides"}, LegendPosition -> {0.9, 0.3},
LegendShadow -> None, LegendOrientation -> Vertical,
LegendSize -> {0.5, 0.3}]
Export["gating.eps", %]

```



gating.eps

```

GatePos = FindRoot[Abs[ $\epsilon$ [t]] == 0, {t, 0}][[1, 2]];
GatePos2 = GatePos fs gate position

a = GatePos + 3;
b = GatePos - 3;

Tgate =
FindRoot[Abs[ $\epsilon$ [t]] == 0.414, {t, a}][[1, 2]] -
FindRoot[Abs[ $\epsilon$ [t]] == 0.414, {t, b}][[1, 2]];
Tgate2 = Tgate fs tgate

e1 = FindRoot[Abs[ $\epsilon$ [t]] == 0.414, {t, b}][[1, 2]];
e2 = FindRoot[Abs[ $\epsilon$ [t]] == 0.414, {t, a}][[1, 2]];

MaxEy = FindMaximum[{Abs[Ey[t]], e1 ≤ t ≤ e2},
{t, GatePos}];
MaxEx = FindMaximum[{Abs[Ex[t]], e1 ≤ t ≤ e2},
{t, GatePos}];

tEx = t /. Last[MaxEx];
tEy = t /. Last[MaxEy];

Abs[Ex[tEy]];

Abs[Ey[tEx]];

0. fs gate position
10.8543 fs tgate

Ix = NIntegrate[(Abs[Ex[t]])^2, {t, -300, 300}];
Iy = NIntegrate[(Abs[Ey[t]])^2, {t, -300, 300}];
Ratio = Iy / Ix
1.34567

ListPointPlot3D[
Table[{Re[Ex[t]], Re[Ey[t]], t},
{t, -150, 150, .01}], PlotRange -> All]

Plot[{Abs[ $\epsilon$ [t]], 0.41, Re[Ex[t]], Re[Ey[t]]},
{t, e1, e2}, PlotRange -> {All, All},
AxesLabel -> {"time (fs)", "Ellipticity"},
BaseStyle -> {FontFamily -> "Times", FontSize -> 16},
PlotPoints -> 30]

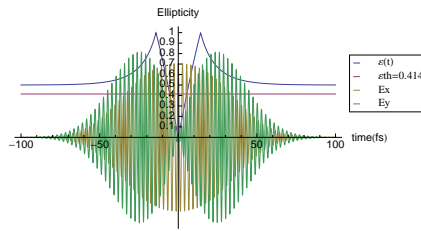
Plot[{(Abs[Ex[t]])^2, (Abs[Ey[t]])^2},
{t, -120, 120}, PlotRange -> {All, All},
AxesLabel -> {"time (fs)", "Intensity"},
BaseStyle -> {FontFamily -> "Times"},
PlotPoints -> 25, PlotLegend -> {"Ix", "Iy"},
LegendPosition -> {0.5, 0.2}, LegendShadow -> None,
LegendOrientation -> Vertical,
LegendSize -> {0.2, 0.3}]

```

```

Plot[{Abs[ε[t]], 0.414, Re[Ex[t]], Re[Ey[t]]},
{t, -100, 100}, PlotRange → {All, All},
AxesLabel → {"time (fs)", "Ellipticity"},
PlotPoints → 170,
BaseStyle → {FontFamily → "Helvetica"},
PlotLegend → {"ε(t)", "εth=0.414", "Ex", "Ey"},
LegendPosition → {0.8, 0}, LegendShadow → None,
LegendOrientation → Vertical,
LegendSize → {0.39, 0.3},
Ticks →
{Automatic, {0.1, 0.2, 0.3, 0.4, 0.5, 0.6,
0.7, 0.8, 0.9, 1}}]

```



*Calculations ;*

```

(*In this part the ratio Ig/Iin is
calculated.*)
Ixgated = NIntegrate[(Abs[Ex[t]])^2,
{t, (GatePos - (Tgate / 2)),
(GatePos + (Tgate / 2))}];
Iygated = NIntegrate[(Abs[Ey[t]])^2,
{t, (GatePos - (Tgate / 2)),
(GatePos + (Tgate / 2))}];
Ipulse2 = NIntegrate[(Abs[2 * Etrans1[t]])^2,
{t, -400, 400}];
GatedRatio2 = ((Ixgated + Iygated) * FWHM) /
(Tgate * Re[Ipulse2])
0.122542

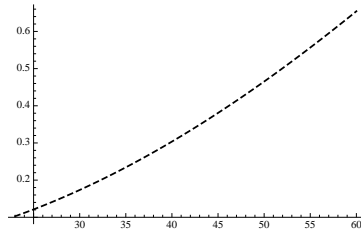
(*rg as a function of Ic/Id=
ratio and the delay between the 2 pulses.*)
εth = 0.414;
B = Sin[(2 * ArcTan[εth])];
rg[delay_, ratio_] :=
((FWHM^2) / (2 * delay)) *
Log2[
((-2 * (1 / Sqrt[ratio]) * Sqrt[(1 - (B^2))]) +
(B * ((1 / ratio) - 1))) /
(B - (2 * (1 / Sqrt[ratio])) + (B * (1 / ratio)))]
rg[15, 1];
rg[60, 0.01];
rg[36.18, 0.25];
datarg = Table[rg[delay, ratio],
{delay, 10, 60, 1}, {ratio, 0.01, 1, 0.05}];

```

```

a1 = Plot[ratiovaluefunction[delay, 10.8543], {delay, 23, 60},
PlotRange -> All, PlotStyle -> {Thickness[.005], Black, Dashed}]
a2 = Plot[ratiovaluefunction[delay, 15.], {delay, 13, 60},
PlotRange -> All, PlotStyle -> {Thickness[.005], Black, Dashed}]
a3 = Plot[ratiovaluefunction[delay, 41.5], {delay, 10, 25},
PlotRange -> All, PlotStyle -> {Thickness[.005], Black, Dashed}]

```



```

b1 = ListDensityPlot[
Table[tg[delay, ratio], {ratio, 0.1, 1, 0.1},
{delay, 10, 60, 0.5}], ColorFunction -> Hue,
Mesh -> False, DataRange -> {{10, 60}, {0.1, 1}},
FrameLabel -> {"delay δ (fs)", "Icon / Ides"},
BaseStyle -> {FontFamily -> "Helvetica",
FontSize -> 15}]

```

```
FinalGraph = Show[b1, a1]
```

```
Export["/Users/dimitris/Desktop/gatedistributiongraph.tiff",
FinalGraph, ImageResolution -> 300]
```

```
/Users/dimitris/Desktop/gatedistributiongraph.tiff
```

```
TotalEnergyratioTable =
```

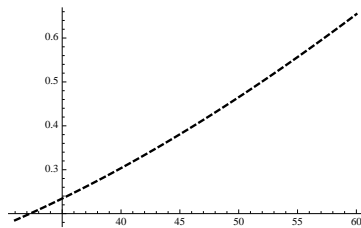
$$\text{Table}\left[\frac{36}{T_{\text{gate}}[d, 36, (\sqrt{\lambda})^{-1}]}, \lambda, .15, 1, .001\right], \{d, 10, 60\};$$

$$\left. \begin{aligned}
& \text{NIntegrate}\left[\text{Igate}[t, d, 36], \{t, -T_{\text{gate}}[d, 36, (\sqrt{\lambda})^{-1}]/2., \right. \\
& \quad \left. T_{\text{gate}}[d, 36, (\sqrt{\lambda})^{-1}]/2.\right] / \\
& \left(\frac{1}{R} * \text{NIntegrate}[\text{Eox}[t, d, 36]^2, \{t, -200, 200\}, \text{MaxRecursion} \rightarrow 12] + \right. \\
& \quad \left. \frac{\left(\frac{1}{\sqrt{\lambda}}\right)^2}{1-R} * \text{NIntegrate}[\text{Eoy}[t, d, 36]^2, \{t, -200, 200\}, \right. \\
& \quad \left. \text{MaxRecursion} \rightarrow 12]\right), \{\lambda, .15, 1, .001\}, \{d, 10, 60\};
\end{aligned}$$

```

a3 = Plot[λ[d, 36, 10.8543]^-2, {d, 31, 60}, PlotRange -> All,
PlotStyle -> {Black, Thick, Dashed}]

```



```

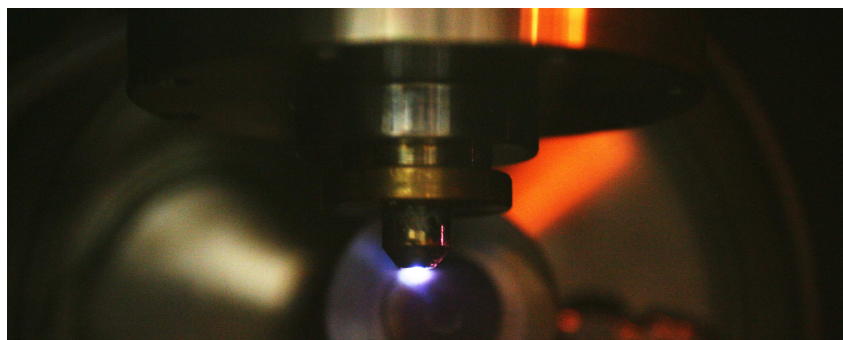
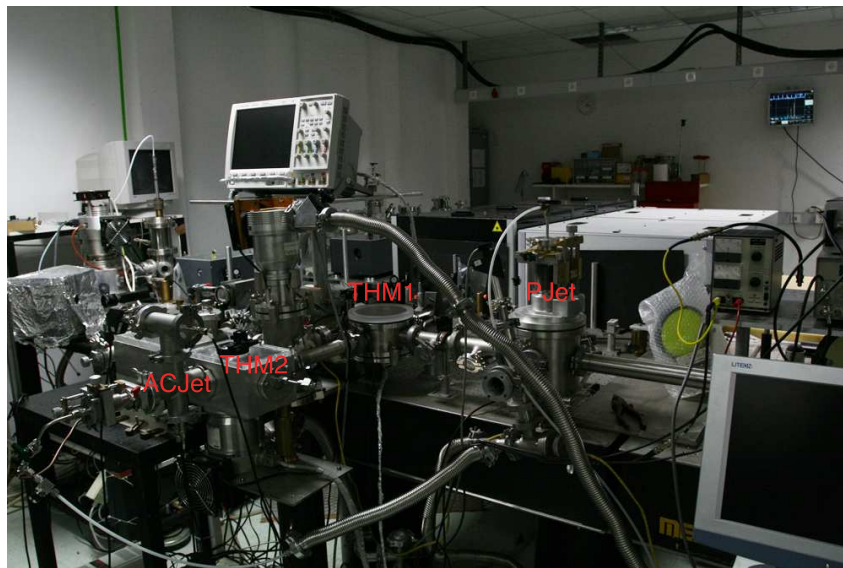
a1 = ListDensityPlot[TotalEnergyratioTable, PlotRange -> All,
ColorFunction -> Hue, Mesh -> False, DataRange -> {{10, 60}, {.18, 1}},
FrameLabel -> {"δ (fsec)", "I_con/I_des"}, ColorFunctionScaling -> False,
LabelStyle -> {FontFamily -> "Helvetica", FontSize -> 14},
FrameLabel -> {"δ (fsec)", "I_con/I_des"}]
(*a2=ListPlot3D[TotalEnergyratioTable, PlotRange->All, ColorFunction->Hue,
ColorFunctionScaling->False, Mesh->False, DataRange->{{20, 80}, {.15, 1}},
LabelStyle->{FontFamily->"Times", FontSize->18},
AxesLabel->{"δ [fs]", "I_c/I_d", "I_g/I_in"}]*)

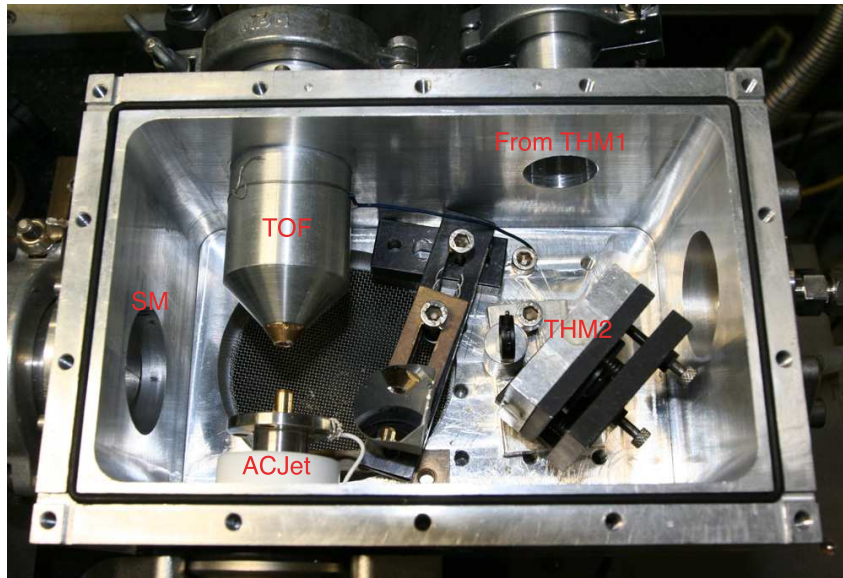
```

```
intgraph = Show[a1, a3]
```

## Appendix B

# Experimental Setup Photographs





# Bibliography

- [1] G Farkas and C Toth. Proposal for attosecond light pulse generation using laser induced multiple-harmonic conversion processes in rare gases. *Physics Letters A*, Jan 1992.
- [2] M Ferray, A L’Huillier, X Li, and L Lompré. Multiple-harmonic conversion of 1064 nm radiation in rare gases. *Journal of Physics B*, Jan 1988.
- [3] A McPherson, G Gibson, H Jara, U Johann, TS Luk, IA McIntyre, K Boyer, and CK Rhodes. Studies of multi-photon production of vacuum ultraviolet radiation in the rare gases. *J. Opt. Soc. Am. B*, (4):595–601, 1987.
- [4] J Seres, P Wobrauschek, C Streli, VS Yakovlev, E Seres, F Krausz, and C Spielmann. Generation of coherent keV x-rays with intense femtosecond laser pulses. *New Journal of Physics*, 8:1–11, 2006.
- [5] E Takahashi, Y Nabekawa, T Otsuka, M Obara, and K Midorikawa. Generation of highly coherent submicrojoule soft x rays by high-order harmonics. *Physical Review A*, 66(2):21802, 2002.
- [6] U Teubner and P Gibbon. High-order harmonics from laser-irradiated plasma surfaces. *Reviews of Modern Physics*, 81(2):445–479, 2009.
- [7] P Corkum. Plasma perspective on strong field multiphoton ionization. *Physical Review Letters*, Jan 1993.
- [8] M Lewenstein, P Balcou, M Ivanov, and AL’Huillier. Theory of high-harmonic generation by low-frequency laser fields. *Physical Review A*, Jan 1994.
- [9] M Protopapas, C Keitel, and P Knight. Atomic physics with super-high intensity lasers. *Rep. Prog. Phys.*, Jan 1997.
- [10] J Krause, K Schafer, and K Kulander. High-order harmonic generation from atoms and ions in the high intensity regime. *Physical Review Letters*, Jan 1992.
- [11] KS Budil, P Salieres, MD Perry, and A L’huillier. Influence of ellipticity on harmonic generation. *Physical Review A*, 48(5):3437–3440, 1993.

- [12] NH Burnett, C Kan, and PB Corkum. Ellipticity and polarization effects in harmonic generation in ionizing neon. *Physical Review A*, 51(5):3418–3421, 1995.
- [13] C Wahlström, J Larsson, A Persson, and T Starczewski. High-order harmonic generation in rare gases with an intense short-pulse laser. *Physical Review A*, Jan 1993.
- [14] TW Hänsch. A proposed sub-femtosecond pulse synthesizer using separate phase-locked laser oscillators. *Optics Communications*, 80(1):71–75, 1990.
- [15] P Tzallas, D Charalambidis, NA Papadogiannis, K Witte, and GD Tsakiris. Direct observation of attosecond light bunching. *Nature*, (426):267–271, 2003.
- [16] Y Nabekawa, T Shimizu, T Okino, and K Furusawa. Conclusive evidence of an attosecond pulse train observed with the mode-resolved autocorrelation technique. *Physical Review Letters*, Jan 2006.
- [17] A Conde, J Kruse, O Faucher, P Tzallas, E. P. Benis, and D. Charalambidis. Realization of time-resolved two-vacuum-ultraviolet-photon ionization. *Physical Review A*, Jan 2009.
- [18] P Paul, E Toma, P Breger, G Mullot, and F Augé. Observation of a train of attosecond pulses from high harmonic generation. *Science*, Jan 2001.
- [19] PB Corkum, NH Burnett, and MY Ivanov. Subfemtosecond pulses. *Optics letters*, 19(22):1870, 1994.
- [20] P Tzallas, E Skantzakis, C Kalpouzos, EP Benis, GD Tsakiris, and D Charalambidis. Generation of intense continuum extreme-ultraviolet radiation by many-cycle laser fields. *Nature Physics*, 3(12):846–850, 2007.
- [21] E Skantzakis, P Tzallas, J Kruse, C Kalpouzos, and D Charalambidis. Coherent continuum extreme ultraviolet radiation in the sub-100-nj range generated by a high-power many-cycle laser field. *Optics letters*, 34(11):1732–1734, 2009.
- [22] M Born and E Wolf. Principles of optics: Electromagnetic theory of propagation, interference and diffraction of light.
- [23] D Rompotis. Third-order, single-shot autocorrelation technique for femtosecond laser pulse characterization. *Undergraduate Diploma Thesis*, 2008.
- [24] P Tzallas, D Charalambidis, NA Papadogiannis, K Witte, and G Tsakiris. Second-order autocorrelation measurements of attosecond xuv pulse trains. *Journal of Modern Optics*, 52(2-3):321–340, Feb 2005.
- [25] O Faucher, P Tzallas, EP Benis, J Kruse, A Peralta Conde, C Kalpouzos, and D Charalambidis. Four-dimensional investigation of the 2nd order volume autocorrelation technique. *Applied Physics B: Lasers and Optics*, 97(2):505–510, 2009.

- [26] NA Papadogiannis, G Nersisyan, E Goulielmakis, TP Rakitzis, E Hertz, D Charalambidis, G.D Tsakiris, and K Witte. Temporal characterization of short-pulse third-harmonic generation in an atomic gas by a transmission-grating michelson interferometer. *Optics Letters*, 27(17):1561–1563, 2002.
- [27] C Lyngå, A L’Huillier, and CG Wahlström. High-order harmonic generation in molecular gases. *Journal of Physics B: Atomic, Molecular and Optical Physics*, 29:3293, 1996.
- [28] NIST Chemistry Webbook. Toluene. *webbook.nist.gov/chemistry*.
- [29] P Agostini and L DiMauro. The physics of attosecond light pulses. *Rep. Prog. Phys.*, Jan 2004.
- [30] F Krausz and M Ivanov. Attosecond physics. *Reviews of Modern Physics*, 81(1):163–234, 2009.
- [31] P Antoine, A L’Huillier, and M Lewenstein. Attosecond pulse trains using high-order harmonics. *Physical Review Letters*, 77(7):1234–1237, 1996.
- [32] W Becker, A Lohr, M Kleber, and M Lewenstein. A unified theory of high-harmonic generation: application to polarization properties of the harmonics. *Physical Review A*, 56(1):645–656, 1997.
- [33] V Strelkov, A Zair, O Tcherbakoff, R López-Martens, E Cormier, E Mével, and E Constant. Generation of attosecond pulses with ellipticity-modulated fundamental. *Applied Physics B: Lasers and Optics*, 78(7):879–884, 2004.
- [34] GD Tsakiris, K Eidmann, J Meyer ter Vehn, and F Krausz. Route to intense single attosecond pulses. *New Journal of Physics*, 8:19, 2006.
- [35] G Sansone, E Benedetti, F Calegari, C Vozzi, L Avaldi, R Flammini, L Poletto, P Villoresi, C Altucci, R Velotta, S Stagira, S De Silvestri, and M Nisoli. Isolated single-cycle attosecond pulses. *Science*, 2006.
- [36] V Strelkov, A Zaïr, O Tcherbakoff, R López-Martens, E Cormier, E Mével, and E Constant. Single attosecond pulse production with an ellipticity-modulated driving ir pulse. *Journal of Physics B: Atomic, Molecular and Optical Physics*, 38:L161, 2005.
- [37] D Oron, Y Silberberg, N Dudovich, and DM Villeneuve. Efficient polarization gating of high-order harmonic generation by polarization-shaped ultrashort pulses. *Physical Review A*, 72(6):63816, 2005.
- [38] SG Rykovanov, M Geissler, J Meyer ter Vehn, and GD Tsakiris. Intense single attosecond pulses from surface harmonics using the polarization gating technique. *New Journal of Physics*, 10:025025, 2008.

- [39] M Gaarde and K Schafer. Space-time considerations in the phase locking of high harmonics. *Physical Review Letters*, Jan 2002.
- [40] C Lyngå, MB Gaarde, C Delfin, M Bellini, TW Hänsch, A L’huillier, and C.G Wahlström. Temporal coherence of high-order harmonics. *Physical Review A*, 60(6):4823–4830, 1999.
- [41] P Antoine, AL’Huillier, M Lewenstein, and P Salières. Theory of high-order harmonic generation by an elliptically polarized laser field. *Physical Review A*, Jan 1996.